CHEMICAL REVIEWS

REVIEW

pubs.acs.org/CR

Optical Studies of Dynamics in Noble Metal Nanostructures

Gregory V. Hartland*

Department of Chemistry and Biochemistry, University of Notre Dame, Notre Dame, Indiana 46556-5670, United States

CONTENTS

1. INTRODUCTION

The past several decades have seen tremendous advances in metal nanoparticle research. This field involves workers from many different areas, including materials scientists interested in synthesizing samples with novel structures and optical properties,[1−10] analytical chemists who develop new molecular sensing schemes,[11−20] biomedical researchers seeking to target and kill cancer cells,[21−28] and engineers interested in creating high speed circuits.[29−32] Many of these applications are inspired by the unique optical properties of metal nanostructures, which derive from the localized surface plasmon resonance (LSPR), a collective oscillation of the conduction electrons that (for spheres) typically occurs in the visible to near-UV region of the spectrum.[33−35] Because many electrons contribute to the LSPR, the absorption and scattering cross sections of metal nanoparticles can be very large.[36,37] The high intensity of the plasmon resonance, and its sensitivity to the environment of the particles and interparticle couplings are at the heart of many of the applications. The plasmon resonance also serves as an optical handle for investigating the properties of the particles themselves.

This review deals with one aspect of the fundamental optical properties of metal nanoparticles: the dynamics that occur following absorption of photons. Rather than being a narrow topic, this is a tremendously diverse subject with many different types of experimental studies. Understanding the sequence of events following photon absorption and their time scales underpins many of the applications of metal nanoparticles. For example, the successful use of metal nanoparticles in photothermal therapy,[21−28] where laser excitation is used to selectively kill cells, is because metals rapidly convert the absorbed photon energy into heat. The different photophysical processes are discussed in chronological order, that is, starting with optical absorption and dephasing of the LSPR, going through internal relaxation of the electrons via electron−electron scattering and electron−phonon coupling, and ending with energy dissipation in the environment.[38−43] The review concentrates on noble metal nanoparticles, as these have been the most studied. There are several reasons for this: recipes are available for making noble metal particles with good control of size and shape,[1−10] the particles are resistant to oxidation, and they have plasmon resonances in the visible to near-IR region of the spectrum,[33−36] so they can be easily studied.

Special Issue: 2011 Plasmonics

Received: August 9, 2010
Published: March 24, 2011

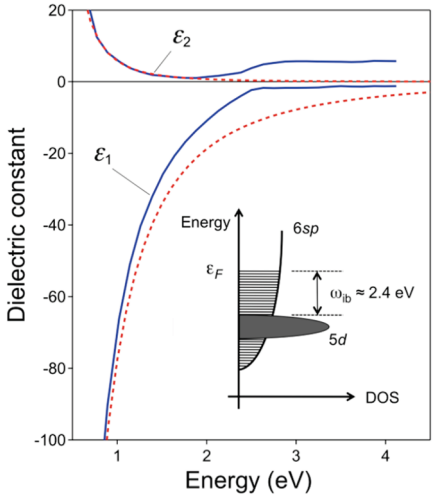

Figure 1. Real and imaginary dielectric constant data for gold (taken from ref 53). The dashed lines show a fit to the data using the Drude model (eq 1). The insert shows a cartoon of the band structure of gold, where ε_F is the energy of the Fermi level, and ω_{ib} is the frequency of the gold interband transitions.

The goal is to describe how the time scales for the different processes are affected by the size, shape and composition of the particles, and the properties of the environment. The effect of these factors on the position of the plasmon resonance has been reviewed elsewhere[33−35,44,45] and will not be discussed in detail here. A significant emphasis will be placed on single particle measurements. This is a relatively new area of study that can provide unique information about electron dynamics in metal nanostructures, and how the environment affects energy relaxation.

2. BACKGROUND

Most chemists are taught a basic understanding of photophysics in terms of separable electronic and vibrational motions, and excited state dynamics that can be described in terms of radiative and nonradiative decay processes, such as intersystem crossing and internal conversion.[46] This zeroth-order picture is helpful for understanding the photophysical properties of semiconductor nanoparticles, with additional effects such as surface recombination of the charge carriers.[40,47−49] However, it breaks down for metal nanostructures. This is because of the high density of empty electronic states at the Fermi level for metals. For metals the starting point for discussing spectroscopy is Mie theory,[33−37,50] which describes the optical response of a spherical particle. Mie theory requires the dielectric constants of the particle and the surroundings as input parameters. The dielectric constants of metals are strongly frequency dependent and contain both real and imaginary components.[51,52] Roughly, the real part determines the position of the LSPR, and the imaginary part determines the dephasing.[33] In this section the basic theory behind the absorption of photons by a metal nanoparticle, and the subsequent energy relaxation processes are discussed.

2.1. Dielectric Constants of Noble Metals

The simplest realistic model for the dielectric constant of a metal is the Drude or free electron model, which was developed to describe DC conductivity.[51,52] For many metals, this model gives reasonable results up to optical frequencies, with suitable modifications because of interband transitions.[53−56] For small particles the dielectric constant is modified by electron-surface scattering, and this can be accounted for semiclassically by adding an extra, size-dependent contribution to the damping constant.[33,57−59]

In the Drude model the conduction electrons are treated as a free electron gas.[51,52] The response to an electric field is obtained by solving the equations of motion for a single electron, and multiplying by the number of electrons per unit volume. This yields the following expression for the dielectric constant:[51,52]

$$\varepsilon(\omega) = 1 - \frac{{\omega_p}^2}{\omega(\omega + i\gamma_b)} \quad (1)$$

where ω_p is the plasma frequency and γ_b is the bulk damping constant that is related to the mean free path l of the electrons by $\gamma_b = v_F/l$ where v_F is the Fermi velocity.[51,52] The plasma frequency is given by $\omega_p = (ne^2/\varepsilon_0 m_e)^{1/2}$, where n is the electron density, ε_0 is the vacuum permittivity, and m_e is the effective mass of the electrons.[51,52] The mean free path of the electrons is limited by scattering off phonons, impurities, etc., with the different contributions adding together according to Matthiessen's rule: $1/l = \Sigma(1/l_i)$, where the l_i are the mean free paths for the individual processes.[33,51] The Fermi velocity and damping constant for bulk Au (for example) are $v_F = 1.4 \times 10^6$ m s^{-1} and $\gamma_b = (15\text{ fs})^{-1}$,[51,53] which implies a mean free path of approximately 20 nm at room temperature.

For a small particle (dimensions less than the bulk mean free path), the damping constant in eq 1 is modified by collisions with the surface[57−59]

$$\gamma(l_{eff}) = \gamma_b + \frac{Av_F}{l_{eff}} \quad (2)$$

where l_{eff} is the effective path length of the electrons (the average distance they travel before scattering off a surface), and A is a constant that depends on the details of the electron-surface interaction.[60,61] The effective path length depends on the size and shape of the particles and can be calculated consistently for different shaped particles by $l_{eff} = 4V/S$ where V is the volume and S is the surface area of the particle.[60,62]

For noble metals like Ag and Au, the Drude model gives a good description of the dielectric constants in the near-IR region of the spectrum, but it breaks down in the visible to near-UV region because of interband transitions.[53,56] The onset of the interband transitions is at ca. 2.4 eV for Au, and 3.9 eV for Ag.[33] The interband transitions give a frequency dependent damping, and can be included in the dielectric constant by adding an extra term[56,63]

$$\varepsilon(\omega) = \varepsilon^{ib}(\omega) + 1 - \frac{{\omega_p}^2}{\omega[\omega + i\gamma(l_{eff})]} \quad (3)$$

where $\varepsilon^{ib}(\omega)$ is the interband contribution. Figure 1 shows a plot of the real (ε_1) and imaginary (ε_2) components of the dielectric constant for bulk Au, where the low frequency response has been fit to the Drude model using eq 1.[56] The imaginary component of the dielectric constant is related to damping, and the presence of interband transitions causes a significant increase in damping at energies greater than 2.4 eV.[33,56] An approximate picture of the band structure of gold is shown in the inset of Figure 1. Physically the increased damping corresponds to scattering of electrons into empty levels of the conduction band (Landau damping).[33,51]

Separating eq 3 into real and imaginary components, and noting that at optical frequencies $\omega \gg \gamma$, gives[64,65]

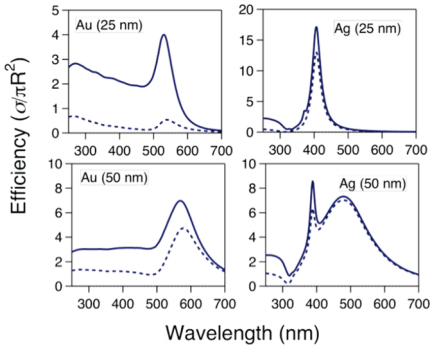

Figure 2. Calculated extinction (solid lines) and scattering (dashed lines) spectra for different sized Au and Ag nanoparticles in water (radii are 25 or 50 nm and $n = 1.33$). Only the dipole and quadrupole terms in eqs 6a and 6b were included.

$$\varepsilon_1(\omega) \approx \varepsilon_1^{\mathrm{ib}}(\omega) + 1 - \frac{{\omega_p}^2}{\omega^2} \tag{4a}$$

and

$$\varepsilon_2(\omega) \approx \varepsilon_2^{\mathrm{ib}}(\omega) + \frac{{\omega_p}^2 \times \gamma(l_{\mathrm{eff}})}{\omega^3} \tag{4b}$$

Equation 4a shows that for small particles $\varepsilon_1(\omega) \approx \varepsilon_1^{\mathrm{bulk}}(\omega)$, that is, the real component of the dielectric constant is essentially the same as the bulk value (there are no terms that involve l_{eff}). However, the imaginary component is modified by electron-surface scattering, and can be written as[65]

$$\varepsilon_2(\omega) \approx \varepsilon_2^{\mathrm{bulk}}(\omega) + \frac{{\omega_p}^2}{\omega^3} \times \frac{A v_F}{l_{\mathrm{eff}}} \tag{5}$$

Thus, for metal nanoparticles the most important effect of decreasing size is increased damping of the electron motion by surface scattering. Note that for calculations, eq 3 should be used for the dielectric constant, not eq 4a or 5, as only modifying ε_2 without changing ε_1 violates the Kramers−Kronig relation.[51] Also, adding an electron-surface scattering term through eq 2 to account for size effects in the optical properties of metal nanoparticles is a phenomenological treatment. There has been recent theoretical work in developing a microscopic explanantion for surface effects based on using a nonlocal dielectric function.[66−68] A discussion of this work is outside the scope of this review.

The electron surface scattering contribution has to be considered when the dimensions of the particles are smaller than the mean free path in the bulk metal, that is, less than 20 nm or so. Note that for very small particles, the spacing between states at the Fermi level becomes larger than kT.[69−72] These particles are no longer metallic in the conventional sense, and the Drude model is not a reasonable approximation to their dielectric function. Transient absorption measurements on these very small particles will be discussed in section 4.4. In particular, these experiments are useful for determining the size where the particle changes from metallic to nonmetallic.[73−75]

2.2. Optical Properties of Small Particles: Mie and Gans Theory

The spectra of metal nanoparticles are dominated by the LSPR. The position of the LSPR depends on the size and shape of the particles, their composition, and the properties of the environment.[33−35,44,45,76] The spectra of spherical particles can be precisely calculated using Mie theory, given that the dielectric constants of the particle and the environment are known.[36,37,50] Mie theory is an exact analytic solution to Maxwell's equations for spheres with an arbitrary size. For rod shaped particles much smaller than the wavelength of light, Gans theory gives an analytic expression that can approximately calculate the spectra.[77−80] For particles with other shapes numerical approaches must be used, such as the discrete dipole approximation (DDA)[81,82] or finite element calculations.[83] Excellent reviews of these different approaches can be found in refs 35, 44, 64, and 84. The line width of the LSPR gives information about the fast electron-scattering processes. There are several contributions to the line width and to understand these different effects it is useful to consider Mie theory calculations for different sized spheres.

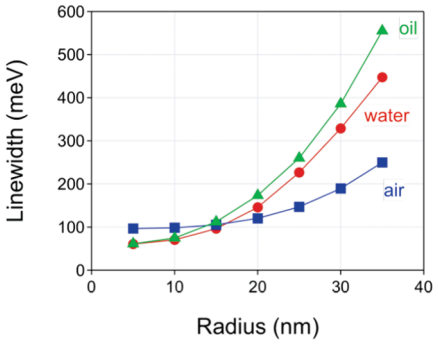

Figure 3. Linewidth of the LSPR versus radius for Ag nanoparticles in different media. The linewidths were obtained from the scattering cross sections versus energy using the full Mie theory calculations. Taken from ref 88 with permission.

The general expressions for the scattering and extinction cross sections from Mie theory are[36,37]

$$\sigma_{\mathrm{sca}} = \frac{2\pi R^2}{x^2} \sum_{n=1}^{\infty} (2n+1)\{|a_n|^2 + |b_n|^2\} \tag{6a}$$

$$\sigma_{\mathrm{ext}} = \frac{2\pi R^2}{x^2} \sum_{n=1}^{\infty} (2n+1) Re[a_n + b_n] \tag{6b}$$

where $x = 2\pi R n_m/\lambda$, n_m is the refractive index of the medium, R is the radius of the particle, and the absorption cross-section is given by $\sigma_{\mathrm{abs}} = \sigma_{\mathrm{ext}} - \sigma_{\mathrm{sca}}$. The a_n and b_n factors are given by[36,37]

$$a_n = \frac{\psi_n'(mx)\psi_n(x) - m\psi_n(mx)\psi_n'(x)}{\psi_n'(mx)\zeta_n(x) - m\psi_n(mx)\zeta_n'(x)} \tag{7a}$$

$$b_n = \frac{m\psi_n'(mx)\psi_n(x) - \psi_n(mx)\psi_n'(x)}{m\psi_n'(mx)\zeta_n(x) - \psi_n(mx)\zeta_n'(x)} \tag{7b}$$

where $\psi_n(z) = (\pi z/2)^{1/2} \times J_{n+1/2}(z)$, $\zeta_n(z) = (\pi z/2)^{1/2} \times (J_{n+1/2}(z) - iY_{n+1/2}(z))$ and $m = n_p/n_m$, where n_p is the refractive index of the particle. The different terms in eqs 6a and 6b correspond to the dipole ($n = 1$), quadrupole ($n = 2$), hexapole ($n = 3$), etc., contributions. Figure 2 shows calculated extinction and scattering spectra for 25 and 50 nm radius gold and silver particles. Only the dipole and quadrupole terms are included in these calculations, as the higher order terms are negligible for this size range. The dielectric constant data was taken from ref 53.

The most noticeable effect when the size of the particles increases is that the plasmon resonance red-shifts and broadens.

dx.doi.org/10.1021/cr1002547 |Chem. Rev. 2011, 111, 3858–3887

The red-shift is a retardation effect, it occurs because the electric field is not uniform across the particle.[36,37] The broadening comes from radiation damping.[85,86] For large particles the coupling between the electrons and the electric field is very strong at the LSPR, so that light scattering is a significant energy loss mechanism.[85,87] This gives rise to an extra damping effect that is not present in the bulk metal. Figure 3 shows a plot of the LSPR linewidths for different sized spherical Ag particles versus radius calculated using eq 6a.[88] The increase in line width arises from radiation damping. The size of the effect is proportional to the volume of the particle, and is stronger in higher dielectric constant environments.[86−88] These calculations show that for Ag nanoparticles radiation damping dominates the line width for particles larger than 20 nm radius.[89,90]

When the particles are much smaller than the wavelength of light (the "quasi-static" limit), only the dipole contributions in eqs 6a and 6b are important, and the extinction is dominated by absorption.[33] In this limit the absorption cross-section is given by[36,37]

$$\sigma_{abs} = 4\pi R^2 x Im\left(\frac{m^2-1}{m^2+2}\right) \quad (8)$$

Using $m^2 = \varepsilon/\varepsilon_m$ where ε is the complex dielectric constants of the particle and ε_m is the dielectric constant of the medium, eq 8 can be rewritten in the more familiar form of

$$\sigma_{abs} = \frac{18\pi V}{\lambda}\varepsilon_m{}^{3/2}\frac{\varepsilon_2}{(\varepsilon_1+2\varepsilon_m)^2+\varepsilon_2{}^2} \quad (9)$$

where V is the volume of the particle.[36,37] eq 9 shows that in the quasi-static limit for spherical nanoparticles the plasmon resonance occurs when $\varepsilon_1 = -2\varepsilon_m$.

A straightforward extension of eq 9 to ellipsoidal particles was developed by Gans[77]

$$\sigma_{abs} = \frac{2\pi V}{3\lambda}\varepsilon_m{}^{3/2}\sum_{j=1-3}\frac{(1/P_j{}^2)\varepsilon_2}{(\varepsilon_1+(1-P_j)\varepsilon_m/P_j)^2+\varepsilon_2{}^2} \quad (10)$$

where the depolarization factors P_j for a cylindrical rod are given by

$$P_A = \left(\frac{1-e^2}{e^2}\right)\left\{\frac{1}{2e}\ln\left(\frac{1+e}{1-e}\right)-1\right\} \quad (11a)$$

$$P_B = P_C = \frac{1-P_A}{2} \quad (11b)$$

and $e = (1-(1/AR)^2)^{1/2}$, where AR is the aspect ratio of the rod (length divided by width). Equations 10 and 11 predict two localized surface plasmon resonances for rod-shaped particles: a longitudinal resonance corresponding to electron oscillation along the major axis of the rod and a transverse band corresponding to electron oscillation across the rod. The longitudinal band occurs in the NIR region, and is sensitive to the aspect ratio of the rod.[78−80]

In the quasi-static limit (that is, when eqs 9 or 10 apply) the line width of the LSPR can be calculated by[33,91]

$$\Gamma = \frac{2\varepsilon_2}{\sqrt{(\partial\varepsilon_1/\partial\omega)^2+(\partial\varepsilon_2/\partial\omega)^2}} \quad (12)$$

For noble metals $|\partial\varepsilon_1/\partial\omega| \gg |\partial\varepsilon_2/\partial\omega|$, so that[91]

$$\Gamma = \frac{2\varepsilon_2}{|\partial\varepsilon_1/\partial\omega|} \quad (13)$$

At frequencies far away from the interband transitions the dielectric function is dominated by the free electron contribution: $|\partial\varepsilon_1/\partial\omega| \approx 2\omega_p{}^2/\omega^3$. In this case, the line width is given by[33]

$$\Gamma = \gamma_b + \frac{Av_F}{l_{eff}} \quad (14)$$

where we have used eq 5 for ε_2. This expression shows that for small particles the LSPR line width is directly related to damping of the free electron motion by intrinsic and surface scattering processes. Equation 14 is an excellent approximation for metal nanoparticles with sizes small enough that radiation damping is unimportant, and with LSPR frequencies displaced from the interband transitions of the metal. When the LSPR is close to the onset of the interband transitions, the bulk damping contribution becomes frequency dependent, and has to be calculated using eq 12.[88]

Radiation damping is often phenomenologically included in line width analysis by adding a volume dependent term to eq 14[85,87−89]

$$\Gamma = \gamma_b + \frac{Av_F}{l_{eff}} + 2\hbar\kappa V \quad (15)$$

where V is the volume and κ is a constant that characterizes the efficiency of radiation damping. This approach is reasonable when the particles are not too large. The factor of 2 in eq 15 arises because radiation damping is considered to be a T_2 process in the literature, whereas the bulk damping and electron-surface scattering are treated as T_1 processes.[87] The relationship between the different time constants is $1/T_2 = 1/2T_1 + 1/T^*$, where T^* denotes pure dephasing contributions.[92] The line width is connected to the dephasing times for the different processes by $\Gamma_i = 2\hbar/T_{2,i}$, where $1/T_{2,rad} = \kappa V$ for radiation damping.[87,89]

The above discussion leads to the following interpretation of optical absorption at the LSPR. The light field excites a dipolar oscillation of the conduction electrons, which rapidly dephases.[33,35] The dephasing time depends on the size of the particle, and is reflected in the line width of the plasmon resonance. For small particles, the line width is broadened by electron-surface scattering, and for large particles radiation damping causes broadening.[33,88] The different functional dependence of the surface scattering and radiation damping contributions on the particle's dimensions leads to a minimum in the LSPR line width for particle sizes on the order of 20 nm.[93] Because the dephasing times are very fast (~10 fs), direct time-resolved measurements of these processes are difficult, although not impossible.[94,95]

2.3. Two-Temperature Model for Electron Cooling

Dephasing of the plasmon resonance through either the intrinsic damping processes of the metal or electron surface scattering leads to absorption of photons.[33,51] This deposits energy into the electron distribution, creating excited electrons that are spread over different levels in the conduction band.[41,96] Energy can also be deposited into the electron distribution by exciting through the interband transitions (to the blue of the LSPR), or the intraband transitions of the metal (to the red of the LSPR).[97] The details of how the electrons are initially distributed

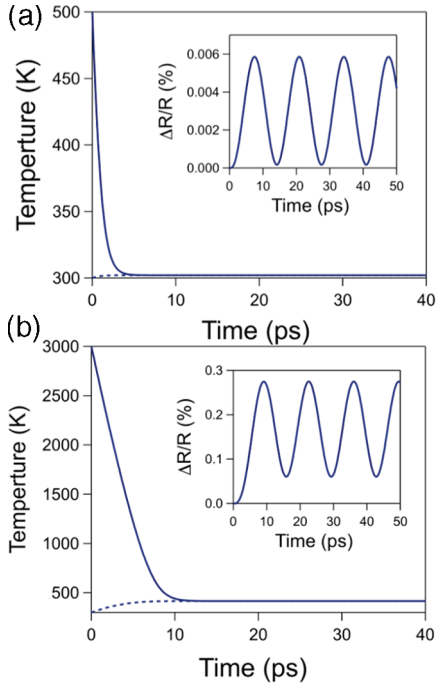

Figure 4. Temperature versus time for Au nanoparticles for an initial electronic temperature of (a) 500 and (b) 3000 K. The inserts show the response of the radius of the particle to laser induced heating. Calculations were performed for Au particles with a 22 nm radius.

over the conduction band levels are different for each case. However, the excited electrons rapidly equilibrate via electron−electron scattering on a few 100 fs time scale to create a hot electron distribution.[98−101] This essentially wipes out any memory of the way the electrons were initially excited. The hot electron distribution then relaxes via phonon emission on a few picosecond time scale.[38−42]

The coupling between the hot electrons and the phonon modes of the particle can be described by the two-temperature model (TTM).[96,102−105] In this model the rate of energy exchange between the electrons and phonons is given by the coupled differential equations

$$C_e(T_e)\frac{dT_e}{dt} = -g(T_e - T_l) \quad (16a)$$

$$C_l\frac{dT_l}{dt} = g(T_e - T_l) \quad (16b)$$

where T_e and T_l are the electronic and lattice temperatures, C_l is the lattice heat capacity, $C_e(T_e) = \gamma T_e$ is the temperature dependent electronic heat capacity,[51,52] and g is the electron−phonon coupling constant.[103,104] The temperature dependence of C_e means that the time scale for electron−phonon coupling depends on the initial electronic temperature.[41,42,103−105] At low excitation levels the relaxation time is given by $\gamma(T_0+\Delta T)/g$, where T_0 is the ambient temperature and ΔT is the temperature increase caused by the pump laser.[42,106,107] Note that at room temperature the electronic heat capacity is much smaller than the lattice heat capacity.[51,52] This means that the initial electronic temperature after laser excitation is much higher than the temperature of the equilibrated electron−phonon system.[41,42,108]

The electron−phonon coupling process in metal nanoparticles has been extensively studied by transient absorption experiments. The goal of these measurements is to determine the electron−phonon coupling constant and to see if this varies with size (for example).[38−41] However, these measurements are tricky, because the relaxation time depends on pump laser intensity. Two approaches have been exploited in the literature to overcome this problem. First, experiments can be performed at very low excitation powers so that the electron distribution is only slightly perturbed ($\Delta T \ll T_0$).[41,109−111] Second, a series of pump laser powers can be used, and the results extrapolated zero power.[106−108] Both techniques yield an estimate of the characteristic electron−phonon coupling time $\gamma T_0/g$.[112] Which method is used depends on what type of laser system is available. Researchers with amplified kHz laser sources have used the extrapolation technique,[38,39,42] and groups with low-power MHz lasers have performed direct measurements at low perturbation of the electron gas.[41,109] The experimental results show that, in general, the electron−phonon coupling time is ∼1 ps for high conductivity metals like Ag, Au, or Cu. It is much faster for metals such as Pt, which have large electron−phonon coupling constants.[105,113]

The increase in lattice temperature from optical excitation is typically a few kelvin to tens of kelvins, although it is possible to melt or even fragment metal nanoparticles at high powers (this occurs when laser excitation causes an increase in lattice temperature of ∼1000 K).[114−119] Figure 4 shows simulations of the change in electronic and lattice temperatures for Au nanoparticles for initial electronic temperatures of 500 and 3000 K, which correspond to laser fluencies of approximately 0.3 mJ/cm^2 and 5 μJ/cm^2, respectively, for excitation at the LSPR maximum. The increase in lattice temperature after the electrons and phonons have reached equilibrium is 2 K in Figure 4a, and 117 K in Figure 4b. These calculations clearly show how the time scale for equilibration between the electrons and phonons varies with initial temperature.[42]

Raising the lattice temperature will cause a small amount of expansion. For particles, the expansion coordinate consists of a linear combination of a few vibrational normal modes.[41,42,120] Importantly, when the dimensions of the particles are larger than 10 nm the time scale for heating, which is a few picosecond at most even for high pump laser powers, is faster than the periods of these vibrational modes. This means that the vibrational modes of the particle that correlate with the expansion coordinate can be coherently excited.[41,42,121−124]

Coherently excited vibrational modes have been detected for a wide range of different size and shaped particles in transient absorption measurements, and the results are discussed in section 5 of this review. A simulation of the change in radius for a 22 nm radius particle is shown in the inserts of Figure 4. In this simulation the breathing mode was modeled as a forced harmonic oscillator, where lattice expansion provides the driving force[125]

$$\frac{d^2R}{dt^2} + \frac{2}{\tau}\frac{dR}{dt} + \left(\frac{2\pi}{T}\right)^2\left\{R - R_0\left(1 + \frac{\alpha}{3}\Delta T_l\right)\right\} = 0 \quad (17)$$

where ΔT_l is the change in lattice temperature calculated through the two-temperature model (eq 16), T is the period of the breathing mode, τ is the damping time (set to be very long in the simulations in Figure 4), R_0 is the initial radius, and α is the coefficient of thermal expansion. This simulation is included to show how the radius of the particle responds to the increase in temperature created by ultrafast excitation. Note that the phase

Scheme 1. Sequence of Events and Approximate Time Scales Following Absorption of Photons by a Metal Nanoparticle

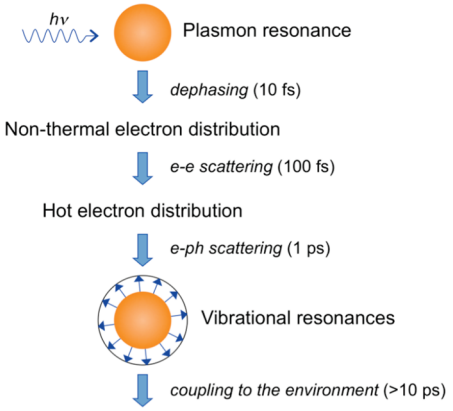

and modulation depth of the oscillations are different in the two simulations. This occurs because the time-scale for electron−phonon coupling and, therefore, the driving force for lattice expansion is longer for higher initial electronic temperatures.

The oscillations in the particle radius from the coherently excited vibrational modes decay by energy transfer to the environment.[126,127] This process is normally masked in ensemble measurements because different sized particles in the sample have different periods, and adding the contributions from all the particles causes an inhomogeneous decay of the signal.[108,128,129] However, the intrinsic damping times can be studied by the recently developed of single particle transient absorption technique.[130−132] These experiments will be discussed in detail in section 5.3.

2.4. Heat Diffusion and Interface Conductance

After the internal electron−electron scattering and electron−phonon coupling process have been completed, the hot particle equilibrates with the environment.[38−42] This process has two components: heat transfer across the interface between the particle and its surroundings, and heat diffusion in the surroundings.[133−137] Heat diffusion within the particle is usually neglected, as this is very fast for metals.[138] For a spherical particle the interface conductance component is described by

$$\frac{\partial T_p}{\partial t} = -\frac{3G}{R\rho_p C_p}(T_p(t) - T_s(R,t)) \qquad (18)$$

where T_p and T_s are the temperatures of the particle and the surroundings, ρ_p and C_p are the density and heat capacity of the particle, and G is the interface thermal conductance. Equation 18 relates the rate of cooling of the particle to the heat flux across the interface.[139] Heat diffusion in the surroundings is described by the diffusion equation, which can be written as[139]

$$\frac{\partial^2(rT_s)}{\partial r^2} = \frac{1}{\alpha_s}\frac{\partial(rT_s)}{\partial t} \qquad (19)$$

for spherically symmetric particles. In eq 19, $\alpha_s = \Lambda_s/\rho_s C_s$ is the thermal diffusivity, where ρ_s, C_s, and Λ_s are the density, heat capacity, and thermal conductivity of the surroundings. Equations 18 and 19 can be solved together using Laplace transform techniques to determine the rate of cooling of the particle.[135−137] In these calculations, the values of the densities, heat capacities and Λ_s are usually taken from the literature, and G is treated as an adjustable parameter.

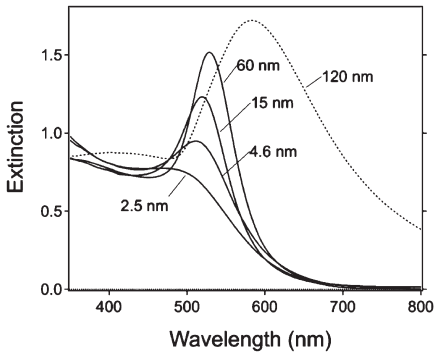

Figure 5. Extinction spectra of different sized Au nanoparticles recorded in aqueous solution (diameters are given in the figure). The particles in these measurements were synthesized using radiation chemistry techniques.[154]

The expressions that result from solving eqs 18 and 19 in the Laplace domain are complex.[135,137] Insight into the cooling process can be obtained from considering the limiting cases of either interface conductance or heat dissipation being the rate limiting step in cooling. When interface conductance is slow compared to heat dissipation in the surroundings, the temperature of the particle decays exponentially with a characteristic time constant of $\tau_i = \rho_p C_p R/3G$. This time scale is 60 ps for a 10 nm radius gold particle, using a value of G = 150 MW m^{-2} K^{-1} (which is typical for gold nanoparticles in water, see below). On the other hand, when heat dissipation is the rate-limiting step in cooling (the interface has a small thermal resistance), then the characteristic time scale for cooling is given by $\tau_d = (\rho_p C_p R)^2/9\rho_s C_s \Lambda_s$.[133,134] For a 10 nm radius particle, the value of τ_d is 30 ps for water. The similar magnitudes of the interface conductance and heat diffusion time scales means that, in general, both these processes have to be considered for nanoparticles in fluids.[133−137] Note that these two processes scale with dimensions in different ways. Thus, studies of different sized particles can in principle allow the interface conductance parameter to be reliably determined.

The description of the sequence of events following optical excitation given above is summarized in Scheme 1. This partitioning of the dynamics into consecutive dephasing (10 fs time scale), electron−electron scattering (100 fs), electron−phonon coupling (1−5 ps), and heat dissipation processes (10−100 ps) is commonly used to discuss experimental data.[38−42] The separation of time scales is not exact, for example, for small particles a significant amount of heat can be deposited into the environment before the electron−phonon coupling process is complete.[140,141] However, it is a very useful starting point for discussing how size, shape, and the environment affect the dynamics of metal nanoparticles.

3. DEPHASING OF THE PLASMON RESONANCE IN METAL NANOPARTICLES

3.1. Ensemble Measurements of Electron-Surface Scattering and Radiation Damping

Experimental observations of spectral broadening from radiation damping date back to the start of the previous century (they were the motivation for Mie's work),[142] and observations of electron-surface scattering were reported over 50 years ago.[143−147]

dx.doi.org/10.1021/cr1002547 |Chem. Rev. 2011, 111, 3858–3887

These effects are relatively easy to see, especially given the advances in synthesis of metal nanoparticles in the past decade.[56,71,148−153] An example of the change in line width of the LSPR with size is shown in Figure 5 for Au nanoparticles in water. The spectra clearly show effects from radiation damping at large sizes, and electron surface scattering at small sizes (<15 nm diameter). In principle, the data in Figure 5 can be used to estimate the electron-surface scattering and radiation damping parameters.[42] However, the measured linewidths are much larger than those calculated from the dielectric constant data of Au, even at sizes where electron-surface scattering and radiation damping are unimportant. This occurs because that the spectra are inhomogeneously broadened, and implies that the electron-surface scattering and radiation damping parameters derived from ensemble measurements are upper limits of the true values and not particularly useful.

For samples of spherical particles, the inhomogeneous broadening most likely arises from the presence of different shaped particles: slight differences in shape have a much larger effect on the position of the plasmon resonance than differences in size.[78] This is also a problem for nanorod samples, where polydispersity in the aspect ratio broadens the longitudinal plasmon resonance.[62,88,93] An interesting system where meaningful line width information has been obtained from ensemble measurements is the Au bipyramids synthesized by Liu et al.[155] These samples have ensemble linewidths that are only ∼30% broader than the single particle linewidths. This is because the position of the longitudinal resonance depends on shape, and the shapes are very uniform in these samples because of the way the particles grow.[155] Liu and co-workers used these materials for refractive index sensing, and demonstrated figures-of-merit for the ensemble sample comparable to single particle measurements.[156] They also showed that the line width decreases by 30% as the temperature of the sample is changed from room temperature to 6 K.[157] This is not because of changes in the occupation of states at the Fermi level, as the longitudinal resonance of the bipyramids occurs in the near-IR, well away from the interband transitions of gold. By careful modeling Liu et al. were able to show that the decrease in line width arises from a decrease in the rate of electron−phonon scattering with temperature.[51,157] This study would be very difficult to do with single particle measurements, because of the technical difficulties of coupling high magnification objectives to low-temperature cryostats.

3.2. Rayleigh Scattering Spectroscopy of Single Particles

The effect of the sample size distribution on the optical spectra can be removed by studying single particles. For metal nanoparticles this can be relatively easily done by recording Rayleigh scattering spectra, using either total-internal reflection[158] or dark-field[87,88,159,160] illumination. There have been a large number of single particle Rayleigh scattering studies of how the size, shape and environment of the particles affect the spectra.[16,17,87,89,90,160−162] The emphasis has been mainly on the position of the LSPR. There have been relatively few studies concerned with teasing out the important factors that control the line width.

3.2.1. Radiation Damping in Noble Metal Nanoparticles. Because Rayleigh scattering is stronger for large particles, it is a natural technique for studying radiation damping. The first single particle studies of radiation damping were performed by Sonnichsen and co-workers.[87,89] They examined gold nanorods with aspect ratios ranging from 2 to 4, and silver and gold spheres

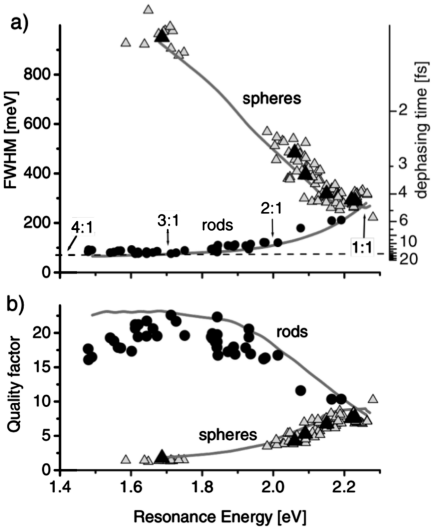

Figure 6. (a) Linewidth versus resonance energy for gold nanorods and nanospheres with different dimensions. (b) Corresponding quality factors for the resonances. Reproduced with permission from ref 87. Copyright 2002 American Physical Society.

with diameters between 20 and 150 nm. For the spherical particles, both the measured scattering spectra and plots of the line width versus resonance frequency showed good agreement with Mie theory calculations.[89] The agreement was better for gold, presumably because of uncertainty in the dielectric constant data for silver.[89] A plot of the line width versus resonance energy for gold nanorods and spheres taken from ref 87 is shown in Figure 6. In the near-IR region, the nanorods have much narrower linewidths for a given resonance frequency. This is because of reduced radiation damping and is simply a volume effect. For spheres, the red shift arises from retardation effects, which are only significant for large sizes. In contrast, for the nanorods the red shift arises from the shape, and not the overall size of the particle. The nanorods used in ref.[87] had relatively small volumes compared to the spheres. Analysis of the line width data using eq 15 gave a value of $\kappa = 4 \times 10^{-7}$ fs^{-1} nm^{-3} for the radiation damping parameter.[87]

Figure 6 shows that the linewidths for the nanorods are essentially the same as those calculated from the bulk dielectric constant data using eq 13.[87] This was also observed in single particle Rayleigh scattering measurements by Liu et al.[62] These results imply that both radiation damping and electron-surface scattering are negligible for nanorods with widths on the order of 15−20 nm. However, increasing the width beyond 20 nm leads to significant broadening.[93,163] Novo and co-workers examined gold nanorods with aspect ratios between 2 and 4, and widths ranging from 8 to 30 nm.[93] Broadening was observed at small sizes because of electron-surface scattering, and at larger sizes because of radiation damping. Fitting the line width data to eq 15 gave a value for the radiation damping parameter of $\kappa = (6.2 \pm 0.5) \times 10^{-7}$ fs^{-1} nm^{-3},[88] in reasonable agreement with the results of Sonnichsen at al.[87] Single silver nanoparticles were examined using correlated optical/electron microscopy experiments by Ginger and co-workers.[164] The electron microscopy measurements allowed them to estimate the volume of the particles, and from this they and derived a value of $\kappa = (1.2 \pm 0.2) \times 10^{-6}$ fs^{-1} nm^{-3} for the radiation damping parameter, slightly larger than the value determined for gold

nanoparticles.[87,93] This difference could be due to differences in the dielectric constants of the two metals, or because the LSPRs for the silver particles in ref.[164] were at higher frequencies, and the efficiency for radiation damping increases with frequency[157,164] because of the $1/\nu^3$ dependence of the density of photon states.[165]

Note that eq 15 is derived for particles sizes that are still in the quasi-static limit, and at some point this approximation will break down. Link and co-workers examined nanorods with aspect ratios between 2 and 3, and widths between 30 and 120 nm.[166] They observed a significant broadening and red-shifting of the dipolar longitudinal LSPR with increasing width, as well as the appearance of higher order modes. The presence of higher order modes implies that eq 15 will not be an appropriate description of the line width.[88] The single particle optical experiments in ref 166 were performed in conjunction with SEM analysis, so that the dimensions of the particles were accurately known. This allowed detailed theoretical modeling of the optical response using DDA calculations.[166] Excellent agreement was obtained between the experimental and calculated spectra, both in terms of the position and width of the resonances.[166] This implies that DDA does a good job of handling radiation damping.[88] Other shapes have also been studied using correlated optical microscopy/electron microscopy experiments.[167−170] In general, if the size and shape of the particles are known, then extended Mie theory calculations[167] or numerical approaches, such as DDA,[35,88,166,168] boundary element method (BEM),[170] or finite-difference time-domain (FDTD)[164,168,171,172] calculations, can reproduce the measured spectra. Correlated optical and electron microscopy studies are a powerful way to study the properties of metal particles; however, it is important to perform the optical measurements before the electron microscopy analysis, as interaction with the electron beam can affect the particles.[173] Thus, it is difficult to use these types of experiments to study how different environments affect the properties of the particles (most electron microscopes are allergic to samples with liquids).

The effect of the environment on the rate of radiation damping is an interesting question. The radiation damping rate is proportional to the refractive index of the surroundings.[85,157,164] Thus, changing the environment around the particles should change the line width. This effect has been seen in single particle measurements for gold nanodisks fabricated by electron beam lithography,[158] and for gold−silver nanoboxes (hollow cubic shaped particles).[174] The particles in these measurements were fairly large, dimensions on the order of 100 nm. Large sizes are needed because radiation damping must make a significant contribution to the line width for this effect to appear. Quantitative analysis of the effect is difficult, because the environment around the particles is asymmetric in typical single particle studies (the particles are usually supported on a glass slide). However, the changes in the line width with added solvent can be reasonable well reproduced by DDA calculations that include the support.[88] Taken together these results show that radiation damping is qualitatively understood for both small particles, where it can be treated as an additive effect in the line width via eq 15, and for large particles where it dominates the line width. However, quantitative understanding is not there yet. Some issues that need to be addressed are the influence the excitation geometry[175−177] and how field enhancement from sharp features (the lightning rod effect) plays into radiation damping.[178,179]

3.2.2. Electron-Surface Scattering. Electron-surface scattering is difficult to study by Rayleigh scattering, as only particles

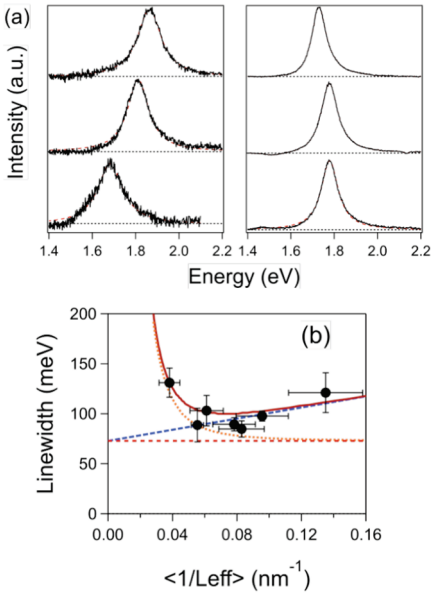

Figure 7. (a) Rayleigh scattering spectra from gold nanorod samples with different average widths. Left: width = 8.1 ± 1.2 nm. Right: width = 14.1 ± 2.1 nm. (b) Average line width versus $1/l_{eff}$ for the different gold nanorod samples. Reproduced with permission from ref 88. Copyright 2008 Royal Society of Chemistry.

that have dimensions on the order of 10 nm or less show significant electron-surface scattering effects, and these particles are typically dim in light scattering measurements. This problem can be overcome by studying nonspherical particles, such as nanorods[62,87,93] or nanoboxes.[174,180] These materials have two important dimensions: for the rods these are length and width, and for the nanoboxes they are edge length and wall thickness. When the width or wall thickness of the particle is reduced below 10 nm, electron-surface scattering effects become important, as they do in spherical particles.[33,35,56−62] However, unlike spheres, because their lengths or edge lengths can be relatively large, the nanorods and nanoboxes can still have reasonable volumes and scatter light efficiently. Thus, dark-field microscopy can be used to examine electron-surface scattering effects for these particles.[62,93,174,180]

Figure 7a shows example Rayleigh scattering spectra for nanorods from two different samples with average widths of 8.1 ± 1.2 nm and 14.1 ± 2.1 nm (error equals standard deviation).[93] For these experiments the length of the rods was adjusted so that the samples all had similar aspect ratios and, therefore, similar longitudinal LSPR frequencies and bulk damping contributions.[88,93] A plot of the average linewidths determined from the single particle measurements versus $1/l_{eff}$ is shown in Figure 7b. The value of l_{eff} was calculated from the average dimensions of the sample, using the $4V/S$ formula derived in refs 60 and 62. The line width shows a minimum for nanorods with widths of approximately 14 nm. The value of the line width at this point is in agreement with the single particle measurements reported in refs 62 and 87. The increase in line width at small $1/l_{eff}$ values (large sizes) is because of radiation damping, and the increase at large $1/l_{eff}$ values (small sizes) arises from electron-surface scattering.[88,93] The curve in Figure 7(b) shows a fit to the data using eq 15, with the individual contributions from electron-surface scattering, bulk damping and radiation damping shown as the dashed/dotted lines. This analysis

yields a surface scattering parameter of $A = 0.30 \pm 0.03$,[88,93] which is in good agreement with results from single particle absorption measurements for gold nanospheres (these experiments are discussed below).[181]

Single-particle Rayleigh scattering spectroscopy has also been used to study electron-surface scattering in hollow gold−silver nanoboxes.[174,180] The measured linewidths for nanoboxes with wall thicknesses on the order of 10 nm are much larger than the linewidths calculated by DDA.[180] This implies an additional broadening contribution beyond bulk damping and radiation damping, as these effects are accounted for in DDA calculations.[35,88] However, eq 15 cannot be used to analyze the data in this case, because the particle sizes are well beyond the range were the quasi-static approximation is expected to be valid. Thus, in ref 88, eqs 4 and 5 were used to add a surface scattering correction to the dielectric function used in the DDA calculations.[88] Spectra were then calculated for different values of the surface scattering parameter, and the calculated linewidths were compared to the average line width from the single particle experiments. This analysis gave a surface scattering parameter of $A = 3.0 \pm 1.1$, which is much larger than the usual values.[33] Possible reasons for this discrepancy are that the $4V/S$ expression for l_{eff} is not appropriate for nanoboxes[88] or that there is significant thinning of the walls in these particles, which does not show up clearly in the TEM analysis. This would lead to an underestimate of the electron-surface scattering effect for a given value of A and, therefore, an overestimate of A in the analysis of the experimental data.[88]

3.2.3. Bimetallic Nanoparticles. For bimetallic core−shell nanoparticles electron scattering can occur not only at the particle solution interface, but also at the interface between the two metals. Liu et al. observed that adding a silver shell to gold nanorods increased the line width from ∼80 to ∼120 meV.[62] These results were interpreted to show that the electron-surface scattering parameter for the gold−silver interface is about 2× larger than that for the particle-solution interface.

Wang et al. examined spherical gold core-silver shell and silver core-gold shell nanoparticles, and the corresponding alloyed particles.[182] They observed essentially no difference in the line width for the alloyed particles compared to the core−shell particles. The linewidths were also close to the values expected from the dielectric constant data, indicating that electron scattering at the gold−silver interface is negligible.[182] However, the LSPR of these spherical particles occurs near the onset of the gold interband transitions, which means that the linewidths are inherently broad, making it hard to observe small changes from additional broadening mechanisms. Sonnichsen and co-workers investigated the linewidths for gold nanorods coated with different thickness silver shells.[183] They observed that at a given resonance frequency, nanorods with thin silver shells have smaller linewidths than the bare gold nanorods. This arises because the imaginary component of the dielectric constant (ε_2) for silver is smaller in the near-IR than that for gold, which means that the intrinsic damping is less for the composite particles.[62,182,183] For thick silver shells the line width increases, presumably because of increased radiation damping.[183]

The results in refs 182 and 183 indicate that electron scattering at the metal−metal interface of core−shell particles is not a significant effect in the dephasing of the LSPR, however, radiation damping does need to be considered. This does not mean that unusual effects do not occur in bimetallic particles. Recently Sonnichsen and co-workers examined alloyed Au−Cu nanorods and showed that the line width was reduced at specific Cu contents.[184] This was attributed to the formation of ordered stoichiometric gold−copper alloys,[184] which have been shown to cause enhanced the DC conductivity in bulk materials.[185]

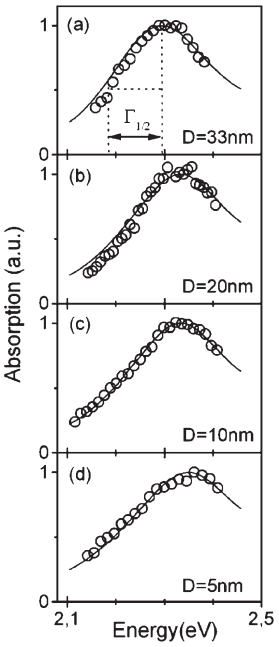

Figure 8. Absorption spectra of small gold nanoparticles recorded using photothermal heterodyne imaging. Reproduced with permission from ref 181. Copyright 2005 American Chemical Society.

3.3. Absorption Spectroscopy of Single Metal Nanoparticles

Because the intensity of scattered light depends on V^2,[36,37] Rayleigh scattering is difficult to see at small sizes. This has led to considerable effort in developing absorption-based techniques for studying small particles.[186−190] Absorption scales as V rather than V^2, and so can be used to detect smaller particles than is possible with Rayleigh scattering.[186,187,191] Absorption based measurements have been used for detection and imaging,[192,193] as well as spectroscopy.[181]

Two main techniques have emerged for interrogating metal nanoparticles through absorption: photothermal heterodyne imaging (PHI),[181,189,191,194] and spatial modulation spectroscopy (SMS).[188,195] In PHI absorption is detected by monitoring the heat deposited in the sample by a modulated pump laser using a nonresonant probe beam.[186,189] In SMS the nanoparticle is moved in and out of the laser beam, and the extinction of the beam is monitored with a lock-in amplifier. Analysis of the SMS signal directly gives the absolute extinction cross-section of the particle.[188,195] These two techniques have advantages and disadvantages. PHI is very sensitive,[193] however, it does not give direct cross-section information,[196,197] and relatively intense pump sources must be used. This last point is not so much a problem for damaging the sample, but can make it technically difficult to record a spectrum. SMS is less sensitive, but a wide range of light sources can be used, such as a white light continuum from a nonlinear optical fiber[198,199] or even a lamp.[200−202] Note that these two techniques monitor different things, PHI is only sensitive to absorption[186,189,194] while SMS monitors extinction of the light beam.[195,198−201]

Lounis and co-workers used PHI to study small gold particles.[181] Example PHI spectra are shown in Figure 8. They

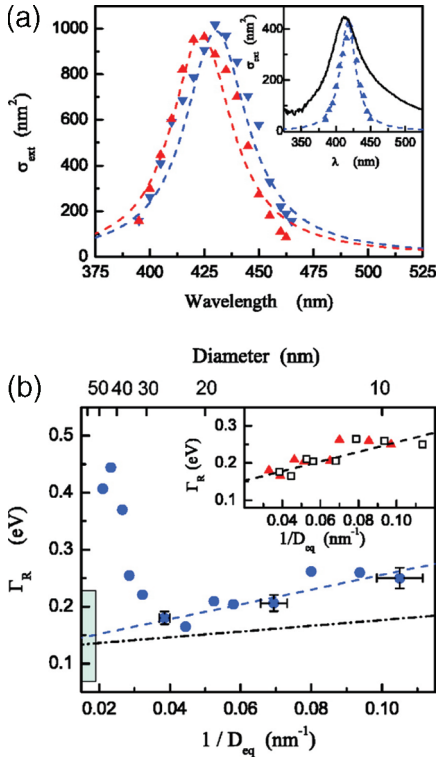

Figure 9. (a) Top: Representative extinction spectra of single Ag@SiO_2 particles recorded using SMS. The solid line in the insert shows the ensemble spectrum (average diameter of the silver core for the sample was 12 nm) (b) Bottom: Linewidth versus 1/diameter for the Ag@SiO_2 particles. Error bars give the uncertainty in the size determination. Reproduced with permission from ref 206. Copyright 2009 American Chemical Society.

were able to measure the resonance energies and half widths of the LSPR for particles with sizes between 33 and 5 nm. Analysis of the data gave an electron-surface scattering parameter of A = 0.33, which is in reasonable agreement with the value for gold nanorods obtained by Novo et al.[88,93] In contrast, Muskens et al. used SMS to measure the absorption spectra of single gold nanorods, and found no evidence of broadening of the longitudinal LSPR from electron-surface scattering.[203] However, the nanorods in these experiments had widths on the order of 15−20 nm, which means that the electron-surface scattering contribution would be very small and hard to detect.[88,93] The measured linewidths in ref 203 were consistent with the Rayleigh scattering studies of nanorods with similar dimensions.[62,87,88,93]

For analyzing electron-surface scattering it is clearly an advantage to know the dimensions of the particle being interrogated. The PHI signal arises from a thermal lens created by the pump laser.[194] Thus, these measurements are typically done with the particles in contact with a liquid that has a strongly temperature dependent refractive index.[189,194,204] The presence of the liquid makes it difficult to perform correlated optical/electron microscopy studies to get precise information about the size and shape of the particles. The Link group has recently demonstrated that PHI experiments can be performed in air, allowing correlated electron and optical microscopy measurements.[205] However, performing experiments in air creates significant inhomogeneities in the environment of the particles. This can cause fluctuations in the signal intensity[205] and the line width,[195] and complicates analysis of electron-surface scattering. On the other hand, the SMS technique gives the extinction cross-section of the particle which, together with spectral and polarization information, allows the size and shape of the particle to be optically determined.[198−201] This in situ size determination means that electron microscopy is not needed in these measurements. This is a significant advantage of the SMS technique, and it allows electron-surface scattering to be studied in detail for single particles in well controlled environments.[206] Note that polarization studies can also be performed with PHI[181,207] and, when combined with spectral information, such measurements can give the aspect ratio of the particle. However, the absolute dimensions cannot be determined directly by PHI, because this technique does not give the absolute absorption cross-section of the particle.

Figure 9 shows extinction spectra and a plot of the line width versus 1/diameter for single Ag nanoparticles coated with SiO_2 recorded using SMS.[206] Silica coated particles were used to ensure a homogeneous environment for the particles.[206] The particles had Ag core sizes ranging from 10 to 50 nm. The diameters in Figure 9(b) were determined by fitting the spectra to extract the size. The insert shows that the details of how the size was determined (fitting the LSPR versus using the integrated area), or the choice of dielectric constants for the metal do not significantly affect the results.[206] The data shows an increase in line width at large sizes because of radiation damping, as well as a significant contribution from electron-surface scattering at small sizes. The line is a fit to the line width data using $2gv_F/R$, which yields g = 0.7 ± 0.1. In terms of eq 14 this corresponds to a surface scattering parameter of A = 0.9 ± 0.1 (l_{eff} = 4R/3 for a sphere). Note that Vallee and Del Fatti have previously shown that the time scale for electron−electron scattering and electron−phonon coupling depend on size for silver.[100,111,208] Taking this effect into account reduces the surface scattering parameter to A = 0.6 ± 0.1. This is slightly larger than the value determined for gold nanoparticles,[88,93,181] but smaller than the value predicted by model calculations.[69,110,209] The ability of SMS to optically determine the size and shape of the particles means that this technique is a powerful tool to study how environment affects electron-surface interactions. These measurements should provide valuable information about effects such as chemical interface damping.[33,34,210]

3.4. Propagating Surface Plasmon Polariton Modes in Metal Nanowires

For extended metal structures propagating surface plasmon polarition (SPP) modes occur in addition to the LSPR.[211] These modes cannot be directly excited with light because of momentum matching considerations.[212] In metal nanowires, propagating SPP modes can be excited by coupling through a prism[213−216] as is done in commercial SPR instruments,[217] by focusing a laser beam at the end of the wire,[218−220] exploiting coupling between the nanowire and a particle,[221,222] coupling to polymer or semiconductor waveguides,[223−226] or by using a tapered optical fiber in a NSOM geometry to launch the propagating SPP modes.[227] Figure 10 shows images of silver nanowires epi-illuminated by a white light source (left panels). The wires scatter strongly, and appear bright on a dark background. The right panels show images where a near-IR pump laser has been focused at one end of the wire.[220] Light emission can be clearly seen at the distal end. In these experiments, the laser excites a propagating surface plasmon polariton mode of the wire, which travels down the wire and re-emits photons at the other end.[218−220]

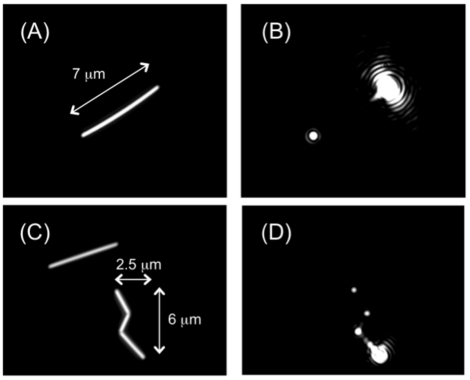

Figure 10. Left: Images of silver nanowires under white light epi-illumination. Right: Images recorded with a near-IR laser (880 nm) focused at one end of the wire. Panels A and B show a straight wire with no kinks or defects, and panels C and D show a kinked wire. Light emission from the distal end and at sharp bends in the wire can be clearly seen. Reproduced with permission from ref 220. Copyright 2008 Wiley-VCH Verlag GmbH & Co. KGaA.

The speed and decay length of the propagating SPP modes can be examined through light scattering measurements. For example, the spectra of the light scattered from the input and output ends of single wires show modulations, which correspond to Fabry−Perot resonator modes.[214−216] Modeling the response gives the dispersion curve for the propagating SPP. The results show that the SPP group velocity varies from 0.6*c* at 1 eV energy to 0.4*c* at 2 eV.[214−216] Similar dispersion curves were obtained by monitoring resonances in the extinction spectra of Ag and Au nanowire arrays.[228] The results are consistent with calculated dispersion curves that take into account the geometry of the nanowires, and the dielectric constants of the metal and the environment.[214−216,228] Analysis of the light scattering spectra also provides information about the decay length of the SPP.[214] The measurements reported in ref 214 gave a decay length of ~10 μm for single crystal nanowires, and showed that it deceases for polycrystalline wires.

The decay length of the propagating SPP modes can also be estimated from images like those shown in Figure 10, by measuring how the intensity of the scattered light decreases with distance.[219,223,227] These measurements allow the decay length to be accurately measured at different wavelengths, which is an advantage compared to the spectral analysis in ref 214. The results in ref 223 gave a decay length of 6.2 μm at 532 nm, 11.3 μm at 633 nm, and 20.2 μm at 980 nm. In comparison, the decays lengths reported in ref 227 were 6.8 μm at 532 nm, 10.6 μm at 633 nm, and 13.3 μm at 980 nm. The slight differences could be due to the different dimensions or environment of the nanowires in the two experiments. The increase in decay length with increasing wavelength is due to the smaller value of ε_2 in the near-IR for noble metals. Note that much longer attenuation lengths, on the order of mm, have been measured for lithographically defined metal waveguides.[229,230] These long attenuation lengths were obtained by carefully designing the system to support coupled surface plasmon polariton modes that have significant field intensity outside the metal.[229,230]

4. ELECTRON THERMALIZATION

The initial ultrafast measurements on metal nanoparticles provided information about the time scale for electron−phonon

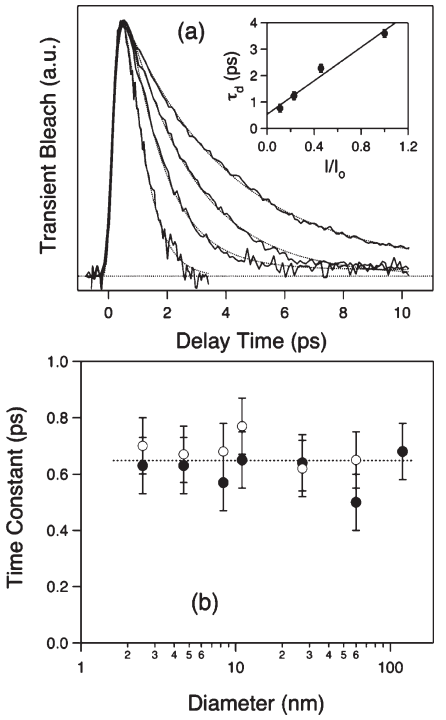

Figure 11. (a) Transient absorption data for Au nanoparticles in aqueous solution (11 ± 2 nm diameter), recorded at different pump laser powers. The insert shows how the decay time varies with relative pump power. (b) Characteristic time scale for electron−phonon coupling plotted against diameter for different gold nanoparticles samples. Closed symbols = intercept, open symbols = fastest measured time scale.[107].

coupling.[231,232,234−237] One of the major goals of these studies was to determine how size, shape, and surface chemistry affect this process. However, as discussed above, the dynamics are intensity dependent, which makes it hard to precisely measure the fundamental electron−phonon coupling time.[106,107] Figure 11a shows transient absorption data for Au nanoparticles collected at different pump fluencies. The insert shows a plot of the electron−phonon coupling time, which was extracted from the data by fitting to an exponential decay, versus the relative pump laser power. Extrapolating the measured time constants to zero power yields an estimate of the fundamental electron−phonon coupling time $\tau_{e\text{-}ph} = \gamma T_0/g$, where g is the electron−phonon coupling constant of the particle. For the experiments in Figure 11a $\tau_{e\text{-}ph}$ = 0.65 ± 15 ps, which yields an electron−phonon coupling constant that is essentially the same as bulk gold.[105,107,112] Figure 11b shows the electron−phonon coupling times measured for different sized gold particles using this technique.

The data in Figure 11 implies that there is no size dependence in the electron−phonon coupling constant.[107] However, the extrapolation technique used to obtain this data is not accurate enough to measure small differences in $\tau_{e\text{-}ph}$: in linear regression the intercept is always less accurate than the slope.[238] A second problem in these measurements is the time-resolution of the experiment. At low excitation levels the electron−phonon coupling time in noble metal nanoparticles is less than 1 ps.[106,107,111,231] This is similar to the time scale for electron−electron interactions (several hundred fs) in silver and gold.[239,240] This makes it hard to separate these two effects,

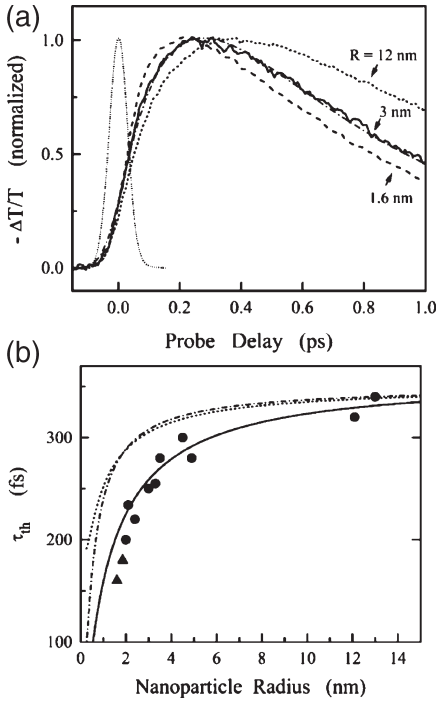

Figure 12. (a) Top: Short time transient absorption data for different sized silver nanoparticles. (b) Bottom: Electron−electron thermalization time extracted from the data in a. Reproduced with permission from ref 100. Copyright 2000 American Physical Society.

especially as both the electron−electron and the electron−phonon interactions are size dependent. A final problem with these experiments is that the choice of probe wavelength can affect the measured time scale, because of the complicated response of the LSPR to electron heating.[41,42,241,242] The difficulties associated with these measurements have created inconsistencies in the literature.

4.1. Size and Shape Dependence of Electron−Electron and Electron−Phonon Coupling

Early transient absorption experiments on Ga and Sn nanoparticles showed a strong decrease in the electron−phonon coupling time (∼50%) as the particle size decreased.[235,236] This was explained in terms of coupling to surface phonon modes,[243,244] which causes an increase in the value of the electron−phonon coupling constant compared to the bulk metal. For noble metal particles a wide range of different results have been reported. Some experiments show no size dependence of the electron−phonon coupling time,[101,106,107,231,232] and some showed that electron cooling is slower at small sizes.[40,73] The most reliable experiments for Ag and Au particles (which have been the most extensively studied) were performed by the Vallee and Del Fatti group using a low power, low noise ultrafast Ti:Sapphire laser system.[100,111] These measurements were conducted in the low perturbation regime, where the electron distribution is only slightly disturbed. The high time-resolution and signal-to-noise in these measurements allowed the electron−electron and electron−phonon coupling processes to be cleanly separated.

Transient absorption traces taken from refs 100 and 111 for different sized Ag particles are presented in Figures 12 and 13. The short time measurements in Figure 12a show the initial rise in the signal. The signal increases as the excited electrons created by the pump laser thermalize among themselves to create a hot

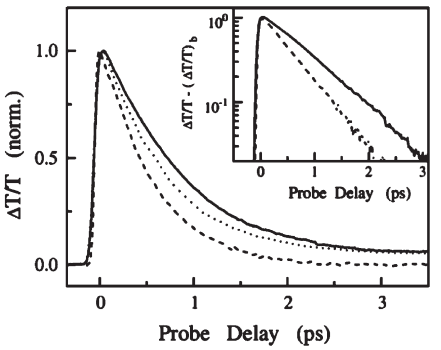

Figure 13. Transient absorption data for different sized Ag nanoparticles. The different curves correspond to particles with diameters of 26 nm (solid line), 6 nm (dotted line), and 3 nm (dashed line). Reproduced with permission from ref 111. Copyright 2003 American Physical Society.

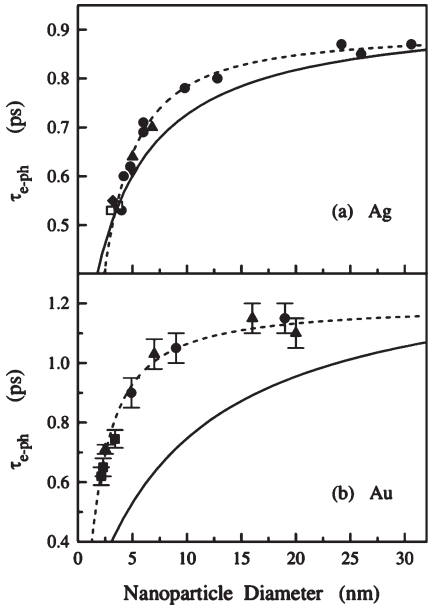

Figure 14. Electron−phonon coupling time versus diameter for (a) silver, and (b) gold nanoparticles. The different symbols correspond to different particle preparations and therefore different environments. Reproduced with permission from ref 111. Copyright 2003 American Physical Society.

electron distribution.[41,208] Fitting the signal to an exponential rise gives a time constant for the electron−electron thermalization process $\tau_{e\text{-}e}$. The value if $\tau_{e\text{-}e}$ is plotted against nanoparticle radius in Figure 12b. The magnitude of $\tau_{e\text{-}e}$ decreases by roughly a factor of 2 as the size of the particles decreases from 26 nm diameter to 3 nm diameter. This effect was attributed to reduced screening between the electrons, because of spill-out of the electron density at the particle surface.[208] Even though the change in $\tau_{e\text{-}e}$ is a large percentage, it is a small absolute value (∼100 fs difference between large and small particles), which means that these measurements are extremely challenging.

Figure 13 shows transient absorption data for different sized Ag particles taken over a slightly longer time range. The decay in the signal now arises from energy loss from the electron distribution because of electron−phonon coupling.[111] The electron−phonon coupling time $\tau_{e\text{-}ph}$ is shorter for small particles,

dx.doi.org/10.1021/cr1002547 |Chem. Rev. 2011, 111, 3858–3887

similar to what was observed for $\tau_{e\text{-}e}$. Figure 14 shows the electron−phonon coupling time versus diameter for different sized Ag and Au nanoparticles. The samples in these measurements were prepared both in solution and in solid matrices.[111] The similarity in the time constant for different preparations implies that the environment does not strongly influence the electron−phonon coupling time. For both Ag and Au $\tau_{e\text{-}ph}$ sharply decreases at sizes less than 10 nm diameter. The decrease in $\tau_{e\text{-}ph}$ was attributed to a similar effect to that for $\tau_{e\text{-}e}$: electron spill-out reduces the average electron density, which results in less screening and an increased interaction between the electrons and the ionic lattice.[111]

An decrease in the electron−phonon coupling time with decreasing size was also observed for small 12 nm diameter Cu particles by El-Sayed and co-workers.[245] However, this effect was attributed to coupling to surface vibrational modes of the particle,[243,244] similar to the mechanism used to explain the decreased electron−phonon coupling time for small Sn and Ga particles.[235,236]

Electron thermalization has also been examined in different shaped particles. Measurements for Au nanorods show electron−electron and electron−phonon coupling times that were very similar to the bulk values.[101,246,247] This is not too surprising, as the diameters of the nanorods used in these experiments are larger than 10 nm, which is the point where size effects become important for $\tau_{e\text{-}e}$ and $\tau_{e\text{-}ph}$, see Figures 12 and 14.[100,111] On the other hand, recent measurements for hollow gold nanoshells (HGNs) have shown faster electron−electron and electron−phonon coupling times compared to bulk gold.[248] The particles in these measurements had very thin metal shells (7 ± 1 nm), and the decrease in $\tau_{e\text{-}ph}$ is therefore most likely a size effect.[248] The picture that emerges from these experiments is that the electron−electron and electron−phonon coupling times are strongly affected by size at dimensions less than ca. 10 nm, but that shape by itself is not an important parameter.

There have also been several studies of how crystal structure affects the electron−phonon scattering process, specifically, comparing the dynamics for single crystal particles to multiply twinned or polycrystalline particles.[249,250] Measurements performed by the El-Sayed group for gold nanoparticles with dimensions on the order of 100 nm showed no effect from crystal structure on the characteristic electron−phonon coupling time $\gamma T_0/g$.[249] However, experiments with small single crystal and multiply twinned Ag nanoparticles (~10 nm diameter) recorded at different pump powers yielded a smaller electron−phonon coupling constant for the single crystal particles.[250] This implies that the defects in the twinned particles increases the coupling between the electrons and phonons. The experiments in both refs 249 and 250 show that the electron−phonon coupling time increases faster with adsorbed energy for the single crystal particles compared to the multiply twinned/polycrystalline particles. This arises because the slope of the time-constant versus adsorbed energy in these experiments is inversely proportional to the electron−phonon coupling constant: a smaller electron−phonon coupling constant means that $\tau_{e\text{-}ph}$ increases faster with pump power.[106,250]

The way the environment of the particles, or the molecules adsorbed to their surface, affect the internal electron thermalization process is an outstanding issue in this area of research. The results in ref 111 imply that the environment has no effect on electron−phonon coupling, however, a limited number of environments were examined in these experiments. Other measurements have shown changes in the electron−phonon coupling time for silver and gold nanoparticles in different environments (both liquids and solids).[251−256] However, these measurements were conducted at relatively high pump laser powers, which introduces some uncertainty in the analysis of the results.[41] This issue should be re-examined with experiments conducted in the low perturbation regime.

4.2. Electron−Phonon Coupling in Multicomponent Particles

Electron thermalization has also been examined in multicomponent metal nanoparticles. The first experiments examined Au−Ag particles, both core−shell particles and alloys,[42,257] and showed essentially no difference in the measured electron−phonon coupling time compared to pure gold or pure silver particles. These experiments were conducted at high pump laser powers, and so were not able to detect small differences in the electron−phonon coupling time with particle composition. More recent measurements performed in the low perturbation regime showed that for Au−Ag particles the electron−phonon coupling time changes linearly with composition for a given size.[258] The particles examined in this work were relatively small (a few nanometers), so that $\tau_{e\text{-}ph}$ for the pure metals was not the same as the bulk.[111] For example, for 2.5 nm diameter particles the electron−phonon coupling time changed from ~0.65 ps for pure Au particles to ~0.48 ps for pure Ag particles.[111] The linear relationship between $\tau_{e\text{-}ph}$ and mole fraction implies that the properties of the composite particles are simply an average of the individual components. More interesting effects were observed for Ni−Ag nanoparticles.[258] In this case the value of $\tau_{e\text{-}ph}$ went through a maximum at approximately 50% Ni composition. This effect is not easily explained.[258] The Ni−Ag particles in ref 258 had a core−shell structure, rather than the alloyed structure for the Ag−Au particles. However, one would expect the presence of an interface between two metals to enhance electron−phonon coupling, not slow it down.

Transient absorption experiments have also been performed for Au−Pt nanoparticles.[113] Representative transient absorption traces are shown in Figure 15a. The addition of a small amount of Pt to Au nanoparticles results in a dramatic decrease in the electron−phonon coupling time. Figure 15b shows a plot of $\tau_{e\text{-}ph}$ versus mole fraction of Au for Pt_{core}−Au_{shell} particles. The data clearly does not follow a linear relationship, which shows that it is not simply the atomic ratios that are important in these measurements.

The curve in Figure 15b shows the effective electron−phonon coupling time calculated as an average of the electron−phonon coupling times of Au and Pt, weighted by the density of electronic states from each[113]

$$\frac{1}{\tau_{e\text{-}ph}} = \frac{\alpha_{Au}}{\tau_{e\text{-}ph}(Au)} + \frac{1-\alpha_{Au}}{\tau_{e\text{-}ph}(Pt)} \quad (20)$$

where α_{Au} is the fraction of electronic states due to Au

$$\alpha_{Au} = \frac{x_{Au} \times \rho(\varepsilon_F)_{Au}}{x_{Au} \times \rho(\varepsilon_F)_{Au} + (1-x_{Au}) \times \rho(\varepsilon_F)_{Pt}} \quad (21)$$

and $\rho(\varepsilon_F)_{Au}$ and $\rho(\varepsilon_F)_{Pt}$ are the density of electronic states at the Fermi level for Au and Pt, and x_{Au} is the atomic mole fraction for Au. Pt has a larger density of electronic states at the Fermi level than Au, because the 5d band falls at the Fermi surface for Pt.[55] This simple phenomenological model reproduces the

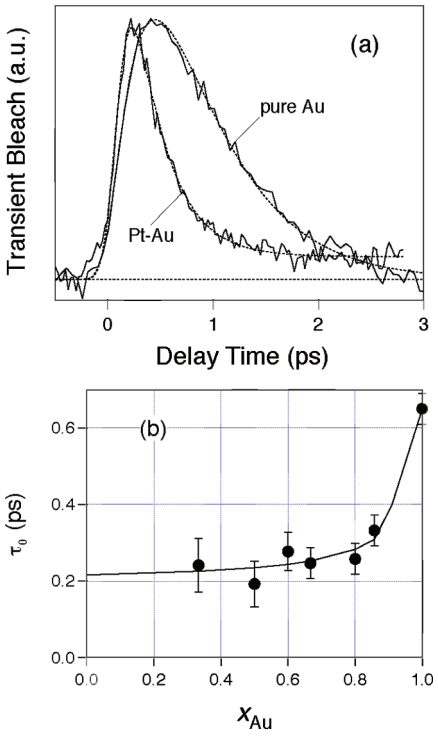

Figure 15. (a) Transient absorption traces for pure Au and Pt−Au nanoparticles (1:0.5 ratio of Pt:Au). (b) Characteristic electron−phonon coupling time $\tau_{e\text{-}ph}$ for Au−Pt nanoparticles versus Au mole fraction. The line is a fit to the data based on averaging the properties of the particles according to the density of electronic states of each metal.

experimental data very well using $\tau_{e\text{-}ph}(Au) = 0.65$ ps, $\tau_{e\text{-}ph}(Pt) = 0.21$ ps, and $\rho(\varepsilon_F)_{Pt}/\rho(\varepsilon_F)_{Au} = 7.3$. In this calculation the values of $\tau_{e\text{-}ph}(Au)$ and $\rho(\varepsilon_F)_{Pt}/\rho(\varepsilon_F)_{Au}$ were taken from the literature,[55,113] and $\tau_{e\text{-}ph}(Pt)$ was allowed to vary. The value of $\tau_{e\text{-}ph}(Pt)$ derived is consistent with conductivity data for bulk Pt.[113] The justification for this model is that electron−phonon coupling is essentially phonon emission from populated electronic states near the Fermi level. Thus, the rate of this process should depend on the density of available electronic states at lower energy. The weighting by electronic states is not an issue for Au−Ag particles because their electron densities are essentially the same (Ag and Au have very similar lattice constants and band structure). In this case, eqs 20 and 21 reduce to a simple weighting of $\tau_{e\text{-}ph}$ according to the atomic molefraction, as observed in ref 258.

4.3. Coupled Metal Nanoparticles

The majority of measurements of electron−phonon coupling have been concerned with isolated particles, as described above. However, it is relatively simple to examine coupled metal particles, either by controlling aggregation or by performing experiments on films. Coupling between metal particles redshifts the LSPR[259] and also produces very high electro-magnetic fields between the particles.[260,261] This makes these systems extremely interesting as substrates for surface enhanced Raman scattering.[262,263]

The first ultrafast studies in this area were performed on Au nanoparticle films. These experiments showed faster dynamics for thicker films.[109] This implies that the time scale for electron−phonon coupling decreases with increased coupling between particles. A decrease in $\tau_{e\text{-}ph}$ with increased interparticle coupling was also observed for Au nanoparticle aggregates in solution.[264] However, experiments on aggregated hollow gold nanoparticles[248] and gold nanoparticle necklaces[265] showed slower electron−phonon coupling times compared to the isolated particles. The samples in these measurements were produced in different ways, and the discrepancy between these results may be because the environment of the particles plays a role in these experiments. As noted above in section 4.1, the way the environment affects the internal electron thermalization of metal nanoparticles is not well understood at this point in time. Another issue in these measurements is that the spectral response of coupled nanoparticles is complicated, and the choice of probe wavelength could have an effect on the dynamics.[41,242]

4.4. Very Small (<2.5 Nm) Metal Nanoparticles

At sizes less than a few nanometers, the spacing between electronic states at the Fermi level becomes larger than thermal energy at room temperature.[71,72] This gives rise to a series of interesting properties, such as Coulomb blockade.[266,267] The optical properties of these small clusters are also very different to their larger counterparts. For example, small gold nanoparticles exhibit discrete features in their absorption spectra, and show relatively strong near-IR luminescence.[71,72,268−275] These are indications of a transition from metallic to semiconducting behavior. This is also reflected in the transient absorption spectra of the small clusters, which show effects from state filling at small sizes,[276] and in the two-photon absorption cross sections.[277] The general consensus from these studies is that gold nanoclusters act like semiconductors at sizes smaller than about 2.2 nm, which corresponds to $Au_{309}(SR)_{92}$ monolayer protected clusters (MPCs).[75,277,278]

The initial ultrafast transient absorption experiments on small gold clusters (Au_{13} and Au_{11} MPCs) showed long excited state lifetimes (>500 ps),[73,279] which are consistent with the observation of emission from these materials. More sensitive measurements on Au_{28} MPCs were able to resolve a fast 750 fs decay in the transient absorption signal, which was independent of the pump laser intensity.[74] The lack of intensity dependence implies that this decay has a different origin compared to the usual electron−phonon coupling process.[41,42] More recent transient absorption measurements for Au_{25} MPCs have shown that the dynamics consists of a < 200 fs relaxation process between excited states of the gold core (a Au_{13} cluster), and a 1.2 ps time scale energy transfer from the gold core to states that involve the peripheral gold atoms and the ligands (ligand semirings).[280] A similar sequence of events was observed for $Au_{24}Pd$ MPCs, but the dynamics were faster: <50 fs relaxation of the core states and 500 fs energy transfer to the ligand semirings.[281] This detailed understanding was made possible by high quality time-resolved optical measurements, as well as the availability of a crystal structure[282] and electronic energy level calculations[283] for the clusters. Fluorescence upconversion has also been used to examine the excited state dynamics of small gold clusters.[75] The results show a fast 220 fs decay for particles smaller than 2.2 nm, which is consistent with the transient absorption results in ref 280.

5. COHERENT EXCITATION OF VIBRATIONAL RESONANCES

The results presented above show that following ultrafast excitation of metal nanoparticles, energy flows out of the electron distribution and into the lattice in a few picoseconds. The exact time scale depends on the initial electronic temperature and the

size and composition of the particles.[41−43,111,113,258] Heating the lattice causes expansion, and for particles larger than a few nanometers, the time scale for heating is faster than the period of the vibrational modes that correlate with the expansion coordinate. This can impulsively excite these modes.[41,42,108,129] The excited modes give rise to modulations in transient absorption traces. This occurs because the vibrational motion causes a small periodic change in the volume or shape of the particles, which shifts the position of the LSPR.[120,122,124,127−129,284]

The contributions from the different modes to the experiment can be evaluated with continuum mechanics.[120,285] To do this, the laser excitation is modeled as an instantaneous isotropic expansion. The time dependent displacement of the particle dimensions $\mathbf{U}(x,y,z,t)$ is expressed as a linear combination over all the normal modes, which form a complete orthogonal basis set

$$\mathbf{U}(x,y,z,t) = \sum_n a_n \mathbf{u}_n(x,y,z)\exp(-i\omega_n t) \qquad (22)$$

where the subscript n refers to the n-th mode, $\mathbf{u}_n(x,y,z)$ is the spatial displacement vector of each mode, ω_n is the radial resonant frequency, and the Fourier coefficient α_n is given by

$$\alpha_n = \int_V \mathbf{u}_n \cdot \mathbf{U}_{t=0} dV \qquad (23)$$

where the integral is performed over the volume of the particle. The modes are normalized such that $\int_V |\mathbf{u}_n|^2 \, dV = 1$. Noting that displacements are infinitesimal within linear elasticity theory, it follows that the temporal response of the change in volume is given by

$$\frac{\Delta V}{V} = \sum_n \gamma_n \exp(-i\omega_n t) \qquad (24)$$

where ΔV is the change in volume, V is the initial volume of the particle, and

$$\gamma_n = \frac{\alpha_n}{V}\int_S \mathbf{n}\cdot\mathbf{u}_n dS \qquad (25)$$

where $\mathbf{n}$ is the outward normal unit vector to the surface S of the particle. Equation 25 represents the contribution from mode n to the expansion.

The integrals in eqs 23 and 25 can be evaluated numerically using finite element analysis. This requires the density and elastic constants for the particle, which can be obtained from standard tables.[286] This analysis makes a prediction of which modes should be excited in transient absorption experiments. Usually the breathing modes of the particle, both the fundamental as well as overtones, are excited.[120,285,287] However, the higher order breathing modes have higher frequencies, and are often hard to detect in transient absorption experiments. This is because the driving force for expansion is not instantaneous, but occurs on a picoseconds time scale dictated by the electron−phonon coupling time of the particle.[126]

5.1. Size and Shape Dependence of the Vibrational Periods

The initial transient absorption studies of the acoustic vibrational modes were performed on spherical nanoparticles.[121−124] In this case the fundamental breathing mode is primarily excited. The period of this mode can be calculated from continuum mechanics using an expression that was first derived in 1882 by Lamb[288]

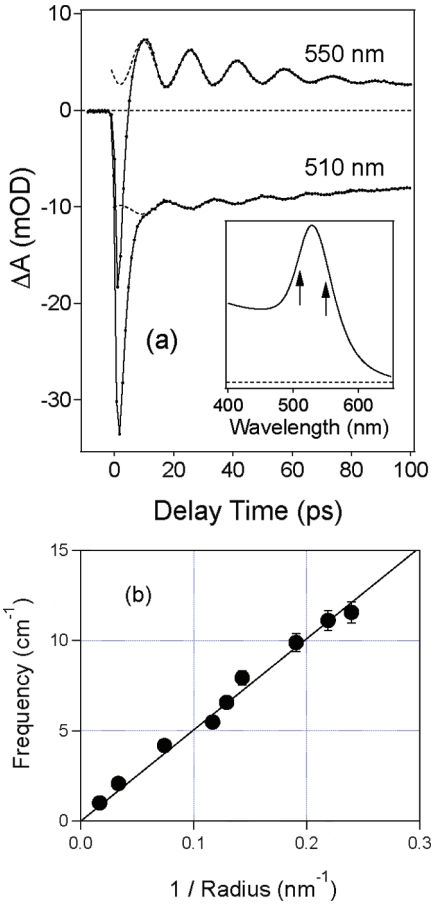

Figure 16. (a) Top: Transient absorption traces for 48 nm diameter gold spheres in water recorded at two different probe laser wavelengths (550 and 510 nm). The insert shows the spectrum of the particles, and the arrows indicate the probe wavelength compared to the LSPR of the sample. (b) Bottom: Frequency versus $1/R$ for different sized Au nanoparticles in aqueous solution. The line was calculated using the elastic constants of bulk gold.

$$T_{\mathrm{br}}^{(n)} = \frac{2\pi R}{\chi_n c_1} \qquad (26)$$

where c_1 is the longitudinal speed of sound of the particle, R is the radius, and χ_n is an eigenvalue that is given by $\chi_n \cot \chi_n = 1-(\chi_n/2\delta)^2$ for a free particle, where δ is the ratio of the transverse and longitudinal speeds of sound.[288] Figure 16a shows example transient absorption traces for Au nanospheres in water recorded with probe wavelengths to the red (550 nm) and blue (510 nm) of the LSPR. The data displays clear modulations that are due to the breathing mode. The phase of the modulations is different for the two traces in Figure 16a. This arises because the LSPR frequency depends on the electron density of the metal.[34] The breathing mode causes a small periodic change in the particle volume, which creates a periodic shift in the position of the LSPR. This causes a 180° phase difference for transient absorption traces collected on different sides of the LSPR.[127,128]

A plot of the measured breathing mode frequencies versus $1/R$ is shown in Figure 16b. The average size of the samples in these experiments was measured by transmission electron microscopy.[124] Frequency versus $1/R$ is plotted in this example rather than period versus R to emphasize the data at small sizes.

dx.doi.org/10.1021/cr1002547 |Chem. Rev. 2011, 111, 3858–3887

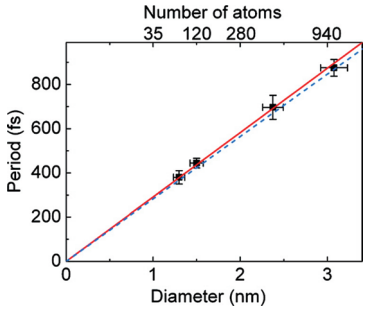

Figure 17. Period versus diameter for Pt nanoparticles produced by low energy cluster beam deposition. The lines show the calculated periods for free particles (red solid line) or particles embedded in silica (blue dashed line). Reproduced with permission from ref 289. Copyright 2010 American Chemical Society.

The line shows the calculated frequency using Lamb's theory (eq 26) with the speeds of sound for bulk gold. The good agreement between the calculations and the experimental data confirms the assignment of the modulations to the breathing vibrational mode of the particles, and shows that the elastic constants of the smallest particles examined in these measurements (~8 nm diameter) are the same as bulk gold.[42,124] Good agreement between Lamb's theory and experimental data was also obtained for spherical Ag nanoparticles in glass with sizes between 5 and 30 nm diameter. This shows that the environment has little effect on the breathing mode frequency.[41]

The size where the continuum mechanics description of the vibrational response breaks down is an interesting question in these measurements. Recently, the breathing modes of very small Pt nanoparticles (between 3 and 1.3 nm diameter) have been interrogated by transient absorption experiments.[289] The periods measured in these experiments are plotted against the diameter of the particles in Figure 17. The particles in these experiments were produced by low energy cluster beam deposition onto a suprasil substrate, with or without a silica coating.[289] The lines in Figure 17 show calculations of the vibrational periods for bare particles (red solid line) or particles embedded in silica (blue dashed line) using an extension of Lamb's theory for particles in a solid matrix.[126] The calculated and experimental periods are in good agreement, which shows that (i) particles with as few as 75 atoms can be described using continuum mechanics with the elastic constants of the bulk material and that (ii) even at small sizes the environment has very little effect on the period (as noted above).[289]

Measurements for very small monolayer protected Au nanoclusters have also been performed,[278,280] but the understanding is less clear. Goodson and co-workers showed that gold nanoparticles smaller than 2.2 nm have size independent vibrational frequencies,[278] suggesting a very different mode is excited at small sizes. Moran and co-workers observed an acoustic vibrational mode for monolayer protected $Au_{25}L_{18}^-$ gold nanoclusters with a similar frequency (2.4 THz) to that in refs 278.[280] Similar results have also been reported for neutral and charged monolayer protected $A_{25}L_{18}$ clusters by Qian et al.[290] Moran and co-workers assigned the 2.4 THz frequency modulations to the breathing mode of the Au_{13} core, modified by mass weighting from the ligands, which include the peripheral Au atoms in the ligand semirings.[280] These results show that Lamb's theory can be applied to very small monolayer protected Au nanoparticles, but that the chemical bonding at the surface may have a significant effect on the vibrational frequencies.[278,280,289] This observation is similar to that for semiconductor quantum dots, where deviations between the experimental frequencies of the acoustic breathing modes and calculated values using the bulk elastic constant data are often seen at small sizes.[291−294] The mass weighting effect from the ligands is particularly large for the experiments in refs 280 and 290 because the ligands involve heavy Au atoms. The experiments in ref 290 also showed a lower frequency (1.2 THz) vibrational mode. Assignment of this mode will most likely require an atomic description of the cluster.

Since the initial experiments on spherical particles, a variety of different shapes have been interrogated by time-resolved measurements. The samples have been produced both by solution phase chemistry, and by lithographic techniques. The solution phase studies include Au and Ag nanorods,[120,295,296] Ag triangles,[297−299] Ag nanocubes,[285] core−shell particles with both metal[300] and dielectric cores,[301,302] hollow cubic shaped particles,[303] Au bipyramids,[127] and nanowires of various metals.[304−308] The lithographically defined particles that have been studied include Au and Ag nanopyramids produced by nanosphere lithography,[309−312] and nanocubes and nanodisks made by electron-beam lithography.[313,314]

For the nanorods both breathing and extensional vibrational modes are excited. Analytical expressions are available for the frequencies of these modes. For a cylindrical rod with a length L and radius R:

$$T_{\mathrm{br}}^{(n)} = \frac{2\pi R}{\varphi_n c_1} \tag{27a}$$

$$T_{\mathrm{ext}}^{(n)} = \frac{2L}{(2n+1)\sqrt{E/P}} \tag{27b}$$

where E is Young's modulus, ρ is the density, and the eigenvalue for the breathing mode is given by $\varphi_n J_0(\varphi_n) = (1 - 2\nu)J_1(\varphi_n)/(1 - \nu)$ where ν is Poisson's ratio. Equations 27a and 27b were derived in the limit that $L \gg R$, and so are strictly only valid for nanorods with reasonably large aspect ratios. The way the breathing modes of a sphere map onto the extensional and breathing modes of a rod with change in aspect ratio has been investigated using finite element analysis.[315]

Analytical expressions are also available for the breathing modes of spherical core−shell particles.[316,317] However, for other shapes the vibrational frequencies must be calculated numerically using finite element analysis. This has been done for cubes,[285] nanotriangles and nanopyramids,[298,312] hollow cubic shaped particles,[303] and bipyramids.[127] Examples of this analysis are presented in Figure 18 and 19. Figure 18a and 18b show the forms of the fundamental breathing mode and the first overtone for a cubic particle. The vibrational frequencies depend on the dimensions of the particle and the elastic constants, and are conveniently expressed as reduced frequencies $\bar{\omega} = \omega L/(E/\rho)^{1/2}$, where L is the edge length of the cube. The value of $\bar{\omega}$ for the breathing mode is $\bar{\omega} = 6.04$, and for the overtone $\bar{\omega} = 9.31$.[285] Note that the finite element calculations were performed for a single crystal Ag cube, whose principal crystal axes were parallel to the edges.[285] This is appropriate for Ag nanocubes produced by wet chemistry techniques.[4] The values of the reduced frequencies depend on crystal structure, and are different for polycrystalline particles, for example. Transient absorption experiments with silver nanocubes of different sizes showed good agreement between the measured periods and calculations for

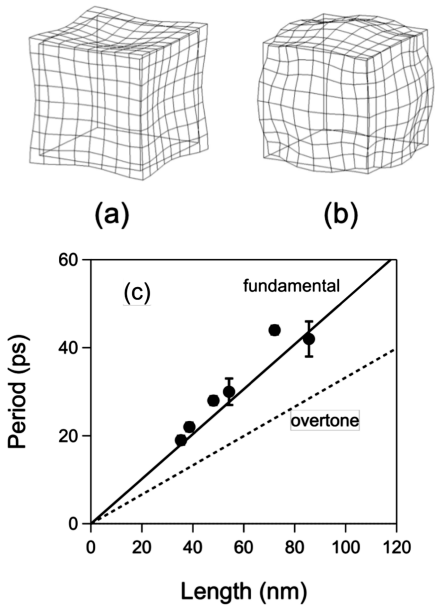

Figure 18. (a) Fundamental and (b) first overtone of the breathing mode for a cubic shaped particle. Reproduced with permission from ref 285. Copyright 2007 American Institute of Physics. (c) Plot of the vibrational period versus average edge length for different nanocube samples.

the fundamental breathing mode. This is shown in Figure 18c, where the period is plotted against the average edge length for different samples.

There is only one dimension for the cubes, so the analysis is fairly straightforward. For the other shapes that have been examined (besides spheres), there are at least two important dimensions. For example, for triangles these are the edge length and height, and for core−shell particles they are the overall size and shell thickness. The vibrational periods calculated from finite element analysis scale with the overall dimensions as $T = 2\pi L/\bar{\omega}(E/\rho)^{1/2}$. However, the exact value of $\bar{\omega}$ depends on the ratio of the different dimensions for the particle.[303,312,315] This is illustrated in Figure 19 where results from finite element analysis for Ag−Au nanoboxes are presented. Figure 19a shows the form of the main vibrational modes that are predicted to contribute to the experiments, and Figure 19b shows how the reduced frequencies of these modes change with the ratio of the edge length to wall thickness (L/w) of the particles.[303] Both these vibrational modes are breathing modes. The size of the symbols in Figure 19b shows the expected contribution of the vibrational mode to the transient absorption experiment calculated via eqs 23−25. Experimental data taken for different samples are shown as the square symbols in Figure 19b. The experiments are again in good agreement with the calculations, both in terms of the vibrational frequencies and the prediction of which mode should be excited in the experiments.[303]

In general, when the analysis is done correctly, there is good agreement between the measured and calculated frequencies.[41,42,127,285,289,296,298,303,312] An exception to this was the report from my group that the vibrational periods for the extensional mode of Au nanorods were significantly longer than the values calculated through eq 27b.[120,318,319] The experimental period versus length data is presented in Figure 20 for two series of experiments: Au nanorods with a [110] growth direction, and nanorods with a [100] growth direction. The solid lines show the

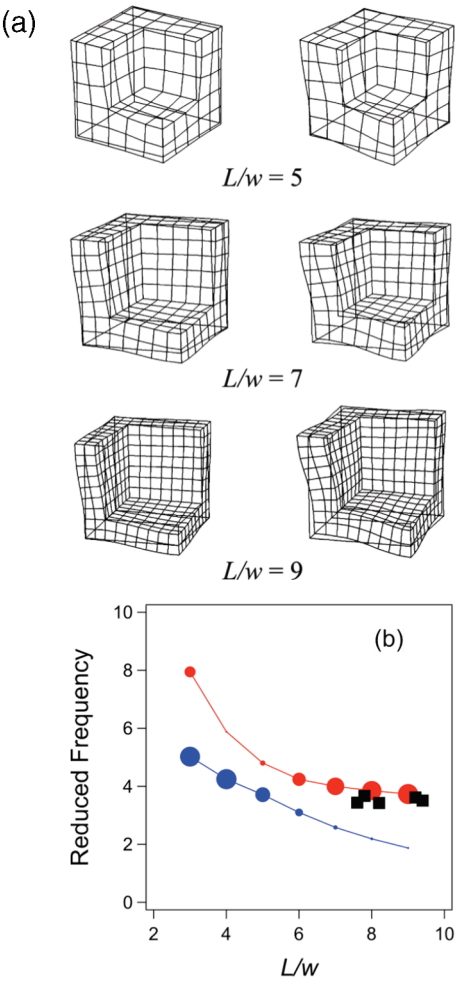

Figure 19. (a) Top: Breathing vibrational modes for hollow cubic shaped particles as a function of edge length to wall thickness ratio L/w (only 1/8 of the box is shown). The lower frequency mode is shown on the left. (b) Reduced frequency versus L/w for the two vibrational modes in a. The circles show the expected contribution of the mode to the experiment, and the square symbols are the experimental frequencies. The size of the circles represents the expected contribution of the mode to the experiment.

calculated periods for the different crystal directions. The values of Young's modulus used in these calculation were $E_{[110]}$ = 42 GPa, $E_{[110]}$ = 81 GPa and $E_{[111]}$ = 115 GPa.[286,318,319] The dashed lines are fits to the experimental data. The data shows a 13% difference between the measured and calculated periods for the [100] nanorods, and a 10% difference for the [110] nanorods. This translates into a 26% reduction in $E_{[100]}$ for the nanorods compared to the bulk value, and a 20% reduction in $E_{[110]}$. A similar softening was also observed for the breathing mode of the [110] nanorods.[318]

There are several systematic errors in these measurements that can affect the results. First, ensemble measurements are biased toward the larger particles in the sample, as these give the strongest transient absorption signal. The larger particles typically have longer lengths and, therefore, lower periods. Second, the laser powers used in these experiments cause a reasonable amount of lattice heating, which decreases the elastic constants of the material. Estimates of the size of these two effects based on the known size distribution of the samples,[319] and the temperature dependence of the elastic constants of gold[286] indicate that half the observed decrease in E for the nanorods could arise from

dx.doi.org/10.1021/cr1002547 |Chem. Rev. 2011, 111, 3858–3887

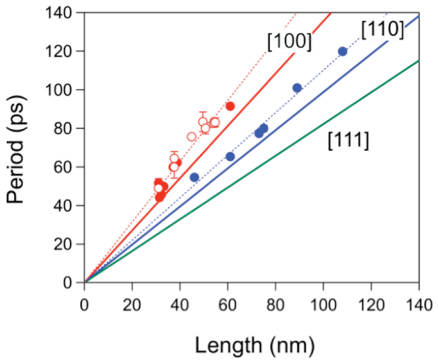

Figure 20. Average period versus average length for gold nanorods with different growth directions. For the [100] nanorods the different symbols correspond to samples produced by different synthetic recipes.[319] Reproduced with permission from ref 319. Copyright 2006 Royal Society of Chemistry.

experimental artifacts. Thus, it is not clear whether the decrease in the extensional mode periods shown in Figure 20 is a real effect. Indeed, transient absorption measurements on single gold nanorods, whose size had been determined by electron microscopy, showed no different between the measured and calculated vibrational periods for the breathing mode.[320] (These experiments will be discussed in section 5.3.3 below.) This implies that these objects have the same elastic constants as the bulk material, counter to the results in Figure 20. Thus, most likely the data in Figure 20 is biased toward larger particles, and does not give correct values for the elastic constants of the nanorods.

On the positive side, the data in Figure 20 nicely demonstrates that crystal structure is an important consideration in the vibrational response of nanostructures. This has to be explicitly included in finite element calculations.[285,303,315] The effect of crystal structure was also examined by Ouyang and co-workers, who measured the period of the breathing mode for single crystal and multiply twinned Ag nanospheres.[250] For particles with similar size, the single crystal particles showed a faster period. The differences correspond to a 37% increase in elastic modulus for the single crystal particles.[250] This leads to the intuitive picture that defects decrease the stiffness of nanomaterials.

As noted above, the vibrational periods measured in the transient absorption experiments also depend on the intensity of the pump laser. This is explicitly shown in Figure 21 for 100 nm diameter gold particles in water. Figure 21a shows the transient absorption data for two different pump laser powers, and Figure 21b shows a plot of the measured period versus the intensity of the pump pulse. The period clearly increases as the pump laser power increases.[321] This arises because the elastic constants of gold decrease with increasing lattice temperature. Figure 21c shows the period versus the lattice temperature, which was calculated from the laser intensity and spot size, the absorbance of the sample at the pump wavelength, and the heat capacity and enthalpy of fusion of gold.[321,322] The line in Figure 21c shows the period calculated using the temperature dependent elastic constants of gold. The break in the line occurs at the bulk melting point of gold. At the melting point, the period for a liquid Au particle is about 15% larger than that for a solid particle (this is mostly due to the reduced speed of sound in liquid Au).[321]

The calculated and experimental periods match well up to the melting point, but the measurements do not show the expected

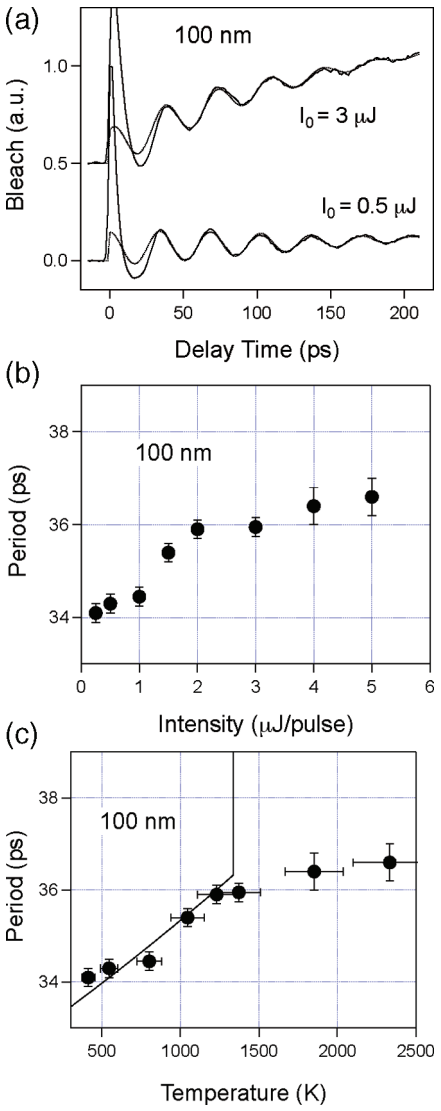

Figure 21. (a) Transient absorption traces for 100 nm diameter gold particles at different pump powers. (b) Period of the breathing mode versus pump intensity. (c) Period versus temperature. The solid line represents the periods calculated from the temperature dependent elastic constants of gold. Reprinted with permission from ref 321. Copyright 2003 American Chemical Society.

increase in period corresponding to melting. This implies that the particles cannot be melted in these experiments. This is most likely due to saturation of the pump laser absorption at high power, as well as nonlinear effects in the pump laser transmission.[321,322] Experiments on the breathing modes of surface supported gold nanoparticles, where the temperature was controlled by heating the substrate, have found evidence of surface melting.[323] However, it has not been possible to observe the breathing mode of liquid metal nanoparticles created by laser induced heating with the pump laser pulse to date.

The good match between the experimental and calculated period versus temperature data in Figure 21 suggests that period of the breathing mode can be used as an internal thermometer.[322,324−327] To do this measurements must first be performed at low powers to determine the period of the breathing mode at close to room temperature. The change in period with power can then be used to estimate the temperature created by

laser induced heating, using the temperature dependent elastic constants of the metal.[322] This is more accurate than estimating the temperature of the particles through calculating the number of adsorbed photons. This technique has been used to examine the damage threshold for gold nanorods[325] and gold−silver nanoboxes.[326] The transient absorption traces for these samples show vibrational modulations up to pump laser powers of about 20 μJ/pulse. The periods become softer at high power, and fitting the data gives a lattice temperature of 970 ± 50 K.[325,326] The observation of vibrational modulations implies that the particles have not undergone any major structural changes on the time scale of the measurements (several hundred ps). At higher powers (greater than 20 μJ/pulse) the modulations disappear, indicating that we have melted the particles.[325,326] The lattice temperatures that can be reached in the transient absorption experiments are much higher than what can be achieved in thermal heating. For example, gold nanorods melt in a few hours at 550 K in an oven.[325] The difference is due to energy transfer to the environment during the laser experiments. At moderate laser powers the particles do not stay hot for long enough for significant structural changes to occur.[325]

At high laser intensities there is a significant amount of heat deposited into the environment. For particles in a liquid this can lead to explosive boiling of the solvent. In transient absorption measurements bubble formation in the solvent is manifested as a rising background signal, which can be seen in the traces recorded at high power in Figure 21a. Power dependent measurements show that the threshold for bubble formation is 550 ± 50 K in water.[324] This temperature correlates very well with the expected temperature for explosive boiling, which is ∼90% of the critical point of the liquid.[328] This effect has also been observed in time-resolved X-ray experiments.[329,330] In these measurements, the structure factors of both the liquid and particle were monitored. The particles show lattice expansion because of heating, and the degree of expansion can be used as an internal measure of the lattice temperature (this is an extremely powerful attribute of the X-ray experiments).[329,330] The solvent shows compression at high pump intensities because of bubble formation.[329,330] The threshold for explosive boiling was found to be 85% of the critical point of water, consistent with the results in ref 324.

The insight from these experiments is that ultrafast excitation of metal nanoparticles can create very high lattice temperatures − well in excess of the boiling point of most solvents. Heat transfer from the particles raises the temperature of the solvent above the boiling point. However, this does not necessarily lead to boiling. Rather the solvent is superheated, and explosive boiling occurs when the temperature reaches ∼90% of the critical temperature of the solvent.[322,324,328−330] These results are relevant to photothermal therapy applications, where heat transfer from laser excited nanoparticles is used to kill cancer cells.[21−27] They are also important for experiments where nanobubbles created by laser excitation of metal nanoparticles are used to enhance imaging in biological systems[331] and where laser heated metal nanoparticles were used for for selectively releasing molecules in cells.[332]

5.2. Excitation Mechanism

In the discussion of electron−phonon coupling and lattice heating given above (Figure 4 and the associated text) the excitation mechanism for the coherent vibrational motion was described as arising from impulsive lattice heating.[41,42] That is, electron−phonon coupling causes a fast step-function like increase in the lattice temperature, which changes the equilibrium size of the particles by an amount $\Delta R/R = \alpha \Delta T_l/3$, where α is the coefficient for thermal expansion. The time scale for heating is faster than the response of the nuclei, which impulsively excites the breathing vibrational mode.

However, impulsive lattice heating is not the complete picture. At high electronic temperatures, the electrons can exert a significant force on the nuclei.[138,333] This is known as hot-electron pressure. The contribution from hot electron pressure to expansion can be seen by writing the coefficient for thermal expansion as[51]

$$\alpha = \frac{1}{B}\left(\lambda C_l + \frac{2}{3}C_e(T_e)\right) \tag{28}$$

where C_e and C_l are the electronic and lattice heat capacities, T_e is the electronic temperature, B is the bulk modulus, and λ is the Gruneisen parameter for the lattice. The first term on the right-hand side gives the lattice contribution to expansion, and the second term corresponds to hot electron pressure. For metals, $C_e \ll C_l$ when the electrons and lattice are in thermal equilibrium, thus, lattice anharmonicity normally dominates expansion.[51] However, in ultrafast experiments all the absorbed energy from the pump laser is initially in the electron distribution. For high pump powers the electronic temperature is very high at short times, see Figure 4 for example, which means that hot electron pressure can make a significant contribution to the driving force for expansion.[126,128,334]

Because the electronic temperature decays rapidly due to electron−phonon coupling, hot electron pressure acts as a delta-function type force on the nuclei. The different time dependence of hot electron pressure compared to lattice expansion (delta-function compared to step-function) affects the phase of the vibrational motion.[126,128,298,334] At high pump laser powers, where hot electron pressure is strongest, the change in phase is on the order of 30° to 45°.[128,334] This can be simulated using the forced harmonic oscillator model, eq 17, with eq 28 for the coefficient of thermal expansion. Good agreement is found between the experimental and simulated phases when hot electron pressure is included in the driving force for expansion.[126,128,334]

The delta function-like time response of hot-electron pressure also means that it is more effective for exciting high frequency vibrational modes compared to lattice expansion. Thus, it makes a stronger contribution to the vibrational response of small particles.[126] For nonspherical particles, where multiple vibrational modes can be excited involving motions along different dimensions, the phase of the higher frequency modes are sometimes observed to be different to that for the low frequency modes.[298,334] This has been seen for Ag triangles[298] and ellipsoidal Ag particles.[334] This effect can be traced to the larger contribution of hot-electron pressure on the driving force for excitation of the higher frequency vibrational modes.[298,334]

5.3. Vibrational Dephasing

The decay of the modulations in the transient absorption traces has several contributions: an inhomogeneous component from the size distribution of the sample, transfer of acoustic energy from the particle to the surroundings,[41,42] and damping because of the surface bound molecules.[127] The first component arises because different sized particles have different vibrational frequencies, and adding the contributions from all the particles

leads to a dephasing of the modulations from the coherently excited vibrational modes. For spherical particles with a Gaussian distribution of sizes, this decay has a $\exp[-(t/\tau)^2]$ form where the decay time is given by

$$\tau = \frac{T}{\sqrt{2}\pi(\sigma_R/\overline{R})} \quad (29)$$

where T is the measured period, and (σ_R/R) is the relative standard deviation of the size distribution.[127,128] Equation 29 was derived for spheres, but it applies to any shape as long as the vibrational period is related to a single dimension, and the experiments probe all the particles in the ensemble. Analysis of experimental data using eq 29 allows the size distribution of the sample to be determined.[128] The component due to energy relaxation has a simple exponential decay, and is more interesting as it provides fundamental information about how the particles interact with their environment.

5.3.1. Theoretical Background for Particles in Solids and Liquids. The theoretical treatment of the damping of the acoustic resonances is not as well developed as the theory for the frequencies. For spheres in a homogeneous solid, the vibrational damping constant γ_n can be calculated by

$$\overline{\omega}_n = \frac{\xi_n c_l^p}{R} = \omega_n + i\gamma_n \quad (30)$$

where the eigenvalue ξ_n is complex and is given by

$$\xi_n \cot \xi_n = 1 - \frac{\xi_n^2}{\eta} \frac{(1 + i\xi_n/\alpha)}{[\xi_n^2 - 4\alpha^2\varepsilon^2(1 + i\xi_n/\alpha)(1 - 1/\eta\beta^2)]} \quad (31)$$

where $\alpha = c_l^m/c_l^p$, $\beta = c_t^m/c_t^p$, $\varepsilon = c_t^m/c_l^m/$, $\eta = \rho^m/\rho^p$, and c_l^i, c_t^i, and ρ^i are the longitudinal and transverse speeds of sound and the density, respectively, of the particle $(i = p)$ or medium $(i = m)$.[126,335] Calculations with eqs 30 and 31 show that the damping depends on the difference in the acoustic impedances $(Z = \rho \times c_l)$ of the particle and the surroundings. When there is a large difference between the acoustic impedances, acoustic energy does not easily transfer from the particle to the surroundings and vibrational damping is slow. In contrast, when there is a small acoustic impedance difference, the acoustic energy in the particle rapidly flows into the environment causing fast damping.[126,220] These calculations also show that the period is relatively insensitive to the environment.[126] This is consistent with transient absorption measurements for silver and platinum spheres in glass, where the measured periods were shown to be the same as those calculated for a free sphere.[41,126,289]

For liquids the relevant parameters are the density and viscosity of the solvent, rather than its acoustic impedance.[127,336] The situation where the viscous boundary layer (the region of the liquid where energy dissipation occurs) is thin compared to the dimensions of the particle (which is the case for metal nanoparticles in low viscosity solvents) has recently been examined in detail.[127] In this case the damping time is proportional to $(\mu\rho)^{1/2}$, where μ and ρ are the viscosity and density of the solvent.[127] Explicit formulas for the damping time are available for spheres,[336] and for thin rods.[127] Note that because the period and damping time both scale with the dimensions of the particle,[126,127,335,336] different samples are best compared through the quality factor of the vibrational resonance $Q = \pi f \tau_1$, where f is the frequency and τ_1 is the homogeneous damping time. This removes the size dependence of the damping and allows the effect of the environment to be examined.

5.3.2. Ensemble Measurements. Typically wet chemistry synthetic methods produce samples with relative polydispersities of (σ_R/R) greater than or equal to 10%. At this level of size dispersity the damping in ensemble transient absorption experiments is dominated by the inhomogeneous decay component, making it difficult to measure the intrinsic homogeneous damping.[128,129] There have been two cases where the homogeneous damping time has been extracted from ensemble measurements. First, Vallee and co-workers examined high quality Ag nanoparticle samples in glass.[126] These samples had relative polydispersities of slightly less than 10%, similar to what is obtained in high quality wet chemistry syntheses. However, because the damping of the acoustic vibrational modes is fairly rapid in glass, the homogeneous damping time could be extracted from the transient absorption measurements. The results were in reasonable agreement with eqs 30 and 31. The experimental damping times scaled linearly with particle size, as predicted by eq 30, but the calculated damping times were slightly smaller than the measured time constant.[126] This is not a problem from sample polydispersity, as this would decrease the measured damping times. Rather the authors attributed the difference to imperfect contact between the particles and the matrix.[126]

The homogeneous damping times of the acoustic vibrational modes of metal nanoparticles in liquids have also been measured by Pelton and co-workers.[127] They examined Au bipyramid samples, which have extremely narrow size distributions. In these experiments the inhomogeneous contribution to the decay was removed using a $\exp[-(t/\tau)^2]$ term, analogous to eq 29. The vibrational periods for the bipyramids depend on two dimensions, length and width, both of which vary from particle to particle. To account for this, finite element modeling was used to estimate the average period $\langle T \rangle$ and standard deviation σ_T for the sample, and the inhomogeneous damping time τ was calculated by $\tau = \langle T \rangle^2/2^{1/2}\pi\sigma_T$.[127] The vibrational quality factors measured in the transient absorption experiments were found to vary from $Q = 17$ for particles in methanol (a low viscosity solvent), to $Q = 1.6$ for glycerol (high viscosity).

To analyze the results, the vibrational damping was separated into solvent dependent effects (viscous damping, Q_{fluid}) and solvent independent effects (intrinsic damping, Q_{int}).[127] The solvent independent effects include internal friction of the Au (the thermoelastic effect),[337] and damping from surface bound molecules. In the study by Pelton and co-workers, the damping from the fluid was calculated using theory developed in the limit of a thin viscous boundary layer, and the intrinsic damping was treated as an adjustable parameter.[127] They found excellent agreement between theory and experiment for an intrinsic damping of $Q_{int} = 25$ for low viscosity solvents (methanol, water and ethylene glycol). Studies of samples with different capping layers indicated that up to 26% of the intrinsic damping arises from the molecules at the particle-fluid interface.[127] The agreement between theory and experiment is not as good for higher viscosity solvents (glycerol), and more work (both experiment and theory) is needed to understand vibrational damping in this case.[127]

5.3.3. Transient Absorption Studies of Single Metal Nanoparticles. The contribution from the size distribution of the sample can be removed by performing transient absorption measurements on single metal nanoparticles. These experiments are technically challenging, as the signal levels are extremely

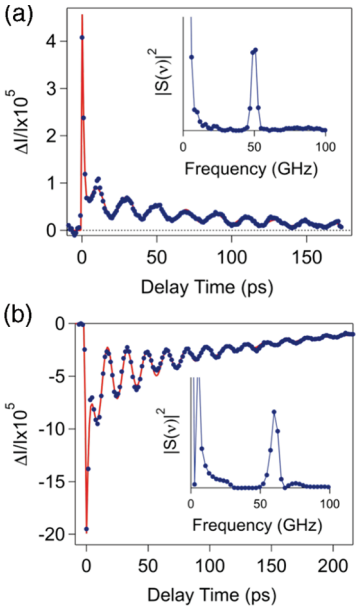

Figure 22. (a) Top: transient absorption trace for a single silver nanocube, taken from a sample with an average edge length of $L = 35 \pm 5$ nm. (b) Bottom: trace for a silver nanowire. The wires in this sample were several micrometers long, and have an average radius of 31 ± 6 nm. Reproduced with permission from refs 339 and 341. Copyright 2009 American Chemical Society and Copyright Royal Society of Chemistry.

small. Single particle transient absorption experiments are performed by focusing the pump and probe beams from a low noise, high repetition rate laser source to a diffraction-limited spot, and detecting the change in transmission of the probe induced by the pump.[130−132] These experiments have been used to study the dynamics of gold[130] and silver nanospheres,[131] pairs of gold nanopyramids,[312] gold nanorods,[320,338] silver cubes,[339] dumbbell shaped gold particles,[340] and silver nanowires.[220,341] All of the samples that have been examined to date are particles that have been fixed on a solid surface (this is because the particles must be kept still for the measurements). The interaction with the surface means that the damping times are relatively fast. Example experimental data for a single silver nanocube and a single silver nanowire are shown in Figure 22. In both cases, modulations from the coherently excited breathing modes can be clearly seen, with damping times that are much longer than that for the corresponding ensemble measurements.[130,339]

Figure 23 shows a scatter plot of the lifetime versus period data for silver nanocubes and silver nanowires taken from refs 339 and 341. This data shows that there is a wide distribution of both the periods and damping times for different particles. The distribution of periods is simply due to the size distribution of the sample.[130,339] This is also seen in studies of single gold nanospheres,[130] single gold nanorods,[320] and gold nanoprism pairs.[312] However, the distribution for the damping times is more complicated. Equation 30 shows that the frequency and damping constant or alternatively the period and damping time scale with dimensions in the same way and, thus, should be strongly correlated. The data in Figure 23 displays a medium correlation between period and lifetime (correlation coefficient = 0.45).[341] The scatter in the data implies that the environment in these experiments plays an important role in the dephasing of the acoustic vibrational modes, and that there is significant heterogeneity in the environment.

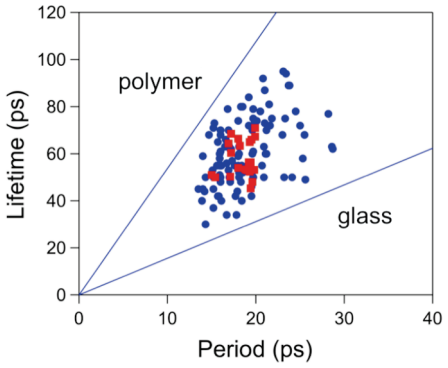

Figure 23. Period versus lifetime data for single silver nanocubes and silver nanowires. The lines show the lifetimes calculated using eqs 30 and 31 for glass and polymer environments. Data taken from refs 339, 341 and used with permission.

The samples in these measurements were prepared by spin coated a polyvinyl alcohol (PVA) solution of the nanoparticles onto a glass coverslip. Thus, the particles are contained in a thin polymer film on glass. The lines in Figure 23 show the damping times calculated using eqs 30 and 31 for Ag particles in glass and polymer environments. The calculations bound the data. This leads to the interpretation that the particles feel a range of different environments. Some particles are in close contact with the glass, and these have strongly damped acoustic vibrational modes. Other particles are in the polymer, and these have long vibrational lifetimes. The distribution of environments leads to the scatter in the lifetime versus period data.[220,339,341] More experiments on samples with better controlled environments are needed to test this hypothesis.

A lack of correlation between the measured dephasing times and the periods of the acoustic vibrational modes has also been seen for single particle transient absorption experiments on gold nanospheres,[130] gold nanorods,[320] and gold nanoprism pairs.[312] (The gold nanorod and gold nanoprism pair experiments were performed without a polymer film.) In all these experiments the particles are in close contact with a solid substrate, and differences in the contact significantly affect the damping time.[220,312,320,339,341] The variation of the damping times is probably most dramatic in the study of gold nanoprism pairs by Burgin et al.,[312] where the vibrational quality factors were found to vary from approximately 5 to 26, with an average quality factor of $Q \approx 12$. These samples were prepared by nanosphere lithography, where thermally evaporated gold is directly deposited onto the substrate. Evidently this produces a wide variation in mechanical contact between the particles and the substrate.[312]

It is interesting to compare the vibrational quality factors measured in the different single particle experiments. The silver nanocubes and nanowires studied in refs 339 and 341 have quality factors of $Q = 10 \pm 2$ (error equals standard deviation). In contrast, the gold nanorods examined in ref.[320] have $Q = 28 \pm 9$ for the extensional mode, and $Q = 37 \pm 6$ for the breathing mode. This implies that for chemically synthesized particles the quality factors are larger for gold than silver. This is consistent with the model of eqs 30 and 31. Gold has a higher acoustic impedance than silver due to its higher density, which means there is a greater acoustic impedance miss-match between the substrate and the particles for gold. This gives rise to longer vibrational damping times for Au. The factor of 3 difference in the vibrational quality factors from refs 320, 339, and 341 is larger than that

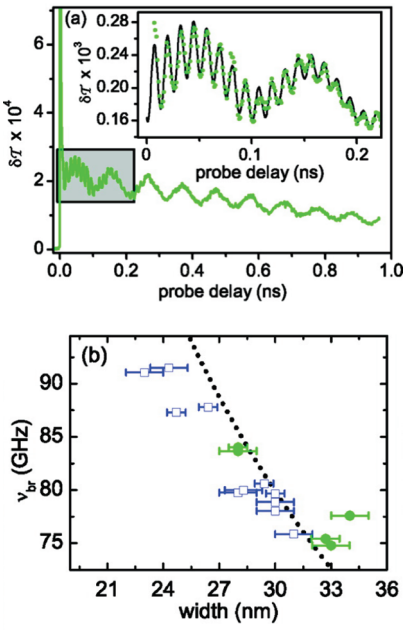

Figure 24. (a) Transient absorption trace for a single gold nanorod displaying modulations from both the extensional mode and the breathing mode. (b) Frequency of the breathing mode from different nanorods plotted against the width determined from electron microscopy. The dashed line represents the calculated frequency using eq 27a. Reproduced with permission from ref 320. Copyright 2008 American Chemical Society.

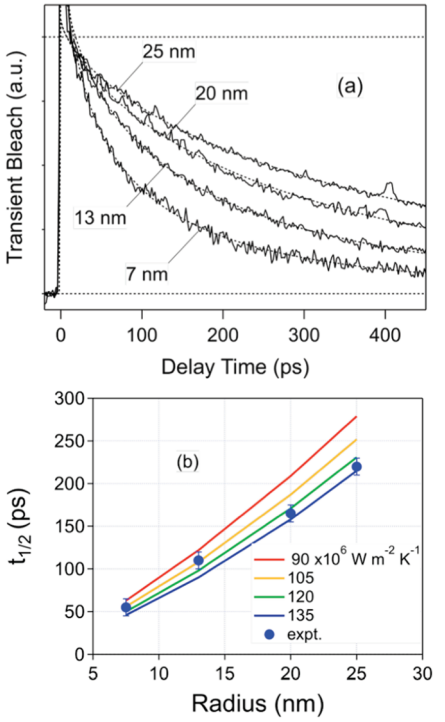

Figure 25. (a) Transient absorption data for different sized gold nanoparticles in aqueous solution. The data have been normalized at the point where the electrons and phonons reach internal thermal equilibrium. The numbers give the radius of the particles. Data taken from ref 140 with permission. (b) Half-time for cooling versus particle radius. The lines represent calculated values of the half-time for different values of the interface conductance.

expected from eqs 30 and 31, implying that other effects from sample preparation may also be important. The quality factors for the gold prisms in ref 312 are similar to that for the silver particles, but these samples are prepared in a different way and, thus, are probably not comparable to the particles synthesized through wet chemistry.

It is also interesting to note that the damping times measured for single gold nanorods in ref 320 (Q values of 30 to 40) are larger than the intrinsic damping determined for gold particles in solution in ref 127 ($Q_{int} \approx 25$). Clearly, if the intrinsic damping were dominated by internal friction, this should not be the case (the quality factors should be limited to $Q \approx 25$). This implies that the molecules at the particle-solution interface probably play a larger role in the intrinsic damping than the 26% contribution determined by Pelton and co-workers.[127] In general, the effect of the interface on vibrational damping for particles in liquids is not well studied, and single particle experiments that probe this would be extremely valuable.

Single particle transient absorption measurements are also useful for measuring the elastic properties of the particles. Orrit and co-workers performed optical measurements on single gold nanorods whose dimensions had been precisely determined by electron microscopy.[320] An example transient absorption trace is shown in Figure 24a. Two modulations appear in the data, the fast modulation is the breathing mode, and the slower modulation corresponds to the extensional mode of the rod.[120] The frequency of the breathing mode is plotted against the dimensions of the nanorods in Figure 24b. The measured frequencies are in good agreement with values calculated using continuum mechanics (eq 27a), which shows that the elastic constants of the nanorods are the same as bulk gold.

The single particle experiments on gold nanorods in Figure 24 contradict the earlier ensemble measurements, see Figure 20 above, which showed differences in the elastic constants of gold nanorods compared to bulk gold.[120,318,319] The discrepancy between the ensemble and single particle measurements is probably due to the effect of the size distribution. For polydisperse samples the periods measured in ensemble transient absorption experiments may not correspond to the average size determined by electron microscopy analysis of the sample. This is because the identity of the particles interrogated in ensemble experiments depend on the details of the pump and probe wavelengths used in the measurement.[120,318,319] Having precise structural information about the specific particle being studied overcomes this problem. This makes the correlated single particle transient absorption/electron microscopy technique a powerful tool for investigating the properties of metal nanoparticles.[320,340]

6. HEAT DISSIPATION AND INTERFACE CONDUCTANCE

The final step in the relaxation process is heat transfer from the particles to the environment.[38−42] This process is longer than the dephasing of the acoustic vibrations described above and has two components: energy transfer across the interface, and heat dissipation in the environment.[133−137] As discussed in section 2.4, the time scales for these two processes are in general similar, which means that it is difficult to separate them. They also depend on dimensions in different ways: for spherical particles the time scale for interface conductance scales as R (the surface-to-volume ratio of the particle), whereas, the heat dissipation

dx.doi.org/10.1021/cr1002547 |Chem. Rev. 2011, 111, 3858–3887

time scales as R^2.[133,134] This means that the cooling dynamics of metal nanoparticles are nonexponential and have a complicated dependence on size and shape. The size dependence is much stronger than that for the faster (and more studied) electron−phonon coupling process. This is shown in Figure 25a, where transient absorption data for different sized gold particles in aqueous solution are presented.[140] The rate of cooling is clearly much faster for the smaller particles.

Early transient absorption experiments established that the rate of cooling increases as the thermal conductivity of the environment increases,[178,253] consistent with heat dissipation in the environment being the rate-limiting step in cooling. Hu and Hartland examined different sized gold particles in water, and found that the relaxation times scale as R^2, again consistent with heat dissipation controlling the rate of cooling.[140] A plot of the half-times for cooling extracted from these experiments is shown in Figure 25b. However, attempts to fit the data using an analytical solution to the heat diffusion equations without interface conductance[342] were not very successful: the calculated and measured time constants were different by a factor of 2.[140] This implies that interface conductance cannot be ignored in these systems.[133−137] Indeed Plech and co-workers examined the size dependent cooling of silver and gold nanoparticles using time-resolved X-ray measurements, and initially concluded that cooling was controlled by interface conductance rather than heat dissipation[343] (in later work they considered both processes).

These results show that both interface conductance and heat dissipation must be considered in the analysis of particle cooling. This requires that the coupled heat transfer equations, eqs 18 and 19, have to be solved together. For spherical particles this can be done using Laplace transform techniques.[135−137] The input parameters needed for these calculations are the heat capacity of the particle and the surroundings, the thermal conductivity of the surroundings, and the interface conductance parameter. Usually the heat capacities and thermal conductivity are taken from the literature, and the interface conductance is adjusted to match the data. An example of this analysis is shown in Figure 25b. The lines represent half-times versus radius calculated for different values of the interface conductance parameter. Comparison to the experimental data implies a value of $G = 110 \pm 20$ MW m^{-2} K^{-1}.[344] This is consistent with the value of $G = 105 \pm 15$ MW m^{-2} K^{-1} measured by Plech and co-workers for gold nanoparticles in water.[135]

In refs 133−135 and 137, the coupled heat transfer equations were used to fit the transient absorption traces, rather than just the half-times as was done in Figure 25b. Fitting the transient absorption traces directly is clearly the better approach. An example of this analysis for AuPd nanoparticles in water stabilized with cetyltrimethylammonium bromide (CTAB) is presented in Figure 26.[134] The value of G derived from this analysis is $G = 230 \pm 50$ MW m^{-2} K^{-1} (the solid line in Figure 26 shows the minimum value of G that can fit the data). Note that the values of G obtained from these measurements include all effects from the interface, that is, coupling between the particle and the surface molecules, energy transport through the surface layer, and coupling between the surface layer and the surroundings. This type of analysis has also been performed for nonspherical particles. However, now the cooling has to be modeled numerically, for example, by using finite element calculations.[345,346]

The majority of the experiments in this area have been for metal particles (usually gold) in water. Cahill and co-workers examined AuPd particles with different passivating layers, and

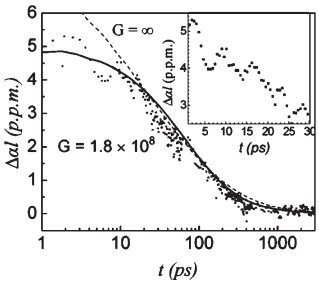

Figure 26. Transient absorption trace for 22 nm diameter AuPd nanoparticles passivated by CTAB in water. The lines show the calculated cooling curves for an infinite interface conductance, and for $G = 180$ MW m^{-2} K^{-1}. The insert shows modulations due to the breathing mode of the particles. Taken from ref 134 with permission. Copyright 2004 American Chemical Society.

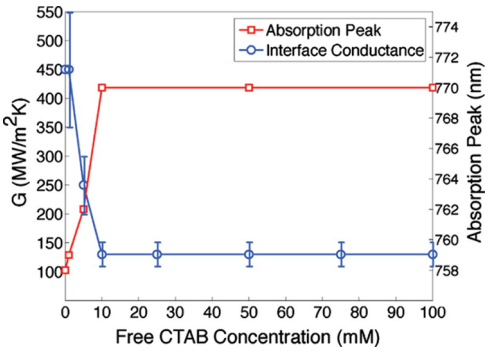

Figure 27. Interface conductance values for gold nanorods stabilized with CTAB, as a function of the free CTAB concentration. The value of G (blue circles) and the position of the longitudinal LSPR (red squares) change around the cmc of CTAB. Reproduced with permission from ref 345. Copyright 2008 American Chemical Society.

found values of the interface conductance parameter between $150 < G < 250$ MW m^{-2} K^{-1}.[134] This is somewhat higher than the values obtained in ref 135 (and also in Figure 25), which could be due to the different identity the molecules at the interface or because the particles are a mixture of Au and Pd, rather than pure Au (Pd was added to the particles in ref 134 to increase the near-IR absorption). This group also examined thiol terminated Au nanoparticles in toluene and found $G = 12$ MW m^{-2} K^{-1}.[133] The much smaller G value for particles in organic liquids was attributed to differences between the coupling of the surface bound molecules to the solvent.[133,134]

The way surface passivation affects interface conductance has been examined in detail by Hamad-Schifferli and co-workers.[345,346] They showed that for CTAB stabilized gold nanorods, the value of the interface conductance depends on the concentration of CTAB in solution.[345] Higher values of G were observed below the critical micelle concentration (cmc) of CTAB. This is shown in Figure 27. The peak of the longitudinal LSPR also depends on CTAB concentration in an analogous way, which indicates that there are changes in the passivating layer of the nanorods around the cmc. The interpretation of this data is that at low concentrations of free surfactant, the CTAB bilayers around the nanorods are incomplete, which leads to water penetration and increased thermal conductivity of the interface.[345]

The Hamad-Schefferli group also examined gold nanorod samples where the CTAB bilayer had been exchanged with

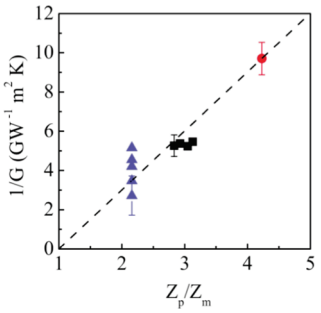

Figure 28. Interface thermal resistance $1/G$ versus the relative acoustic impedance of the particles and the medium Z_p/Z_m. The blue triangles correspond to different sized silver particles, the black squares are Au−Ag alloyed particles, and the red circle is a Au nanoparticle sample. Taken from ref 137 with permission. Copyright 2009 American Physical Society.

different passivating molecules: several different chain length mercaptocarboxylic acids, thiolated polyethylene glycol (PEG), and polyelectrolyte multilayers.[346] For short chain length mercaptocarboxylic acids, or for the PEG/polyelectrolyte passivated surfaces, the G values were effectively infinite, showing that interface conductance is extremely fast. For the longer chain length mercaptocarboxylic acids (greater than C11), the values of G are ~170 MW m^{-2} K^{-1}, consistent with previous measurements.[134,346] These results were again interpreted in terms of water penetration in the passivating layer. The longer chain length mercaptocarboxylic acids exclude water from the interface and give slower interface conductance times. For the short chain length mercaptocarboxylic acids, or the PEG/polyelectrolyte stabilized nanorods, there is significant water penetration, leading to higher interfacial thermal conductivities.[346] Increased interfacial thermal conductivity from solvent penetration has also been observed for core−shell gold nanoparticles, both for polymer shells[347] and for silica coated particles.[348]

Overall these results show that for surface passivated metal nanoparticles in water, the typical value of the interface conductance parameter is $G \approx 100 - 200$ MW m^{-2} K^{-1}, with higher values (faster heat transfer) obtained when the passivating layer allows solvent penetration.[345,346] The cooling dynamics of different sized Ag, Au, and Au−Ag alloyed nanoparticles in glass has also been examined by Crut and co-workers.[137] In these experiments the interface conductance was found to depend on the difference in acoustic impedance between the particle and the surroundings, similar to the situation for damping of the acoustic vibrational modes of metal nanoparticles.[126] A plot of the interface thermal resistance ($1/G$) versus the relative acoustic impedance of the particles and the medium (Z_p/Z_m) is shown in Figure 28. The relative acoustic impedance was varied by changing the composition of the particles (using different mole ratios of Au and Ag), and by using different types of glass. The data for pure Ag particles (blue triangle in Figure 28) show considerable variation between samples. This was attributed to differences in the nanoparticle-glass contact,[137] which is also the reason why the measured dephasing times of the acoustic vibrational modes of metal nanoparticles in glass are longer than the values calculated using eqs 30 and 31.[126] Interestingly, the magnitude of the interface conductance measured for these systems is similar to that for metal particles in solution (a few hundred MW m^{-2} K^{-1}). The linear relationship between $1/G$ and Z_p/Z_m implies that cooling in this system arises from coupling to the acoustic phonon modes of the glass.[137]

7. FUTURE DIRECTIONS

Broadly speaking, the ways the different dynamical process in metal nanoparticles, dephasing of the LSPR, electron−electron scattering and electron−phonon coupling, coherent excitation and damping of acoustic vibrational modes and particle cooling, depend on the size, shape and composition of the particles are reasonably well-known. In particular, the internal electron thermalization processes have been extensively studied and are well understood. However, work remains to be done on understanding the interaction between the particles and their environment. For example, controlled measurements of how surface bound molecules affect the electron dynamics (especially dephasing of the LSPR) are still needed, and a quantitative understanding of cooling and vibrational dephasing is not available at present.

Because the interactions with the environment are inherently heterogeneous, single particle studies are needed to make progress in this area of research. Single particle absorption experiments are an especially promising way to investigate the dephasing of the LSPR of metal nanoparticles, as smaller sizes can be accessed than is possible with light scattering measurements.[181] These experiments also allow the size and shape of the particles to be determined optically, without resorting to electron microscopy.[206] This is important, as electron microscopy measurements can damage the particles (if done first), and are difficult to do in combination with liquids (if done second). Transient absorption studies of single metal nanoparticles is also a relatively unexplored area of research at present,[130,131] and can potentially provide interesting information about particle cooling and the dephasing of the acoustic vibrational modes.[320,341] As the laser sources for these measurements improve, it will become possible to study smaller particles, and possibly get to the size range that is accessible to molecular dynamics simulations.[344,349−351] This would yield a molecular-level understanding of the important factors that control energy transfer to the surroundings. Having a quantitative theory for energy transfer would allow single particle transient absorption experiments to be used as a probe of the microenvironment of thin films, for example.

AUTHOR INFORMATION

Corresponding Author

*E-mail: ghartlan@nd.edu.

BIOGRAPHY

Prof. Hartland obtained his B. Sc. (Hons.) degree from the University of Melbourne (Australia) in 1985, and a Ph. D. degree

from the University of California, Los Angeles in 1991 (under the direction of Prof. Peter Felker). He performed postdoctoral research with Prof. Hai-Lung Dai at the University of Pennsylvania, before joining the University of Notre Dame as an Assistant Professor in 1994. He was promoted to Associate Professor in 2000 and Full Professor in 2004. Prof. Hartland's current research interests are in using optics to study the properties of metal and semiconductor nanostructures, particularly, single particle measurements. He is a member of the Editorial Advisory board of *Chemical Physics Physical Chemistry* (2005−present) and a Senior Editor of *The Journal of Physical Chemistry* (2009−present).

ACKNOWLEDGMENT

This work has been supported by the National Science Foundation of the United States, the Petroleum Research Fund administered by the American Chemical Society, and the University of Notre Dame Faculty Research Program. The author is very grateful to the students who have contributed to this project (especially Jose Hodak, Min Hu, Ignacio Martini, and Hristina Staleva), and to the collaborators who have supplied samples and ideas: Younan Xia (Washington University), Jorge Perez-Juste and Luis Liz-Marzan (University of Vigo), and Paul Mulvaney and John Sader (The University of Melbourne).

REFERENCES

(1) Henglein, A. *Chem. Rev.* **1989**, *89*, 1861.
(2) Storhoff, J. J.; Mirkin, C. A. *Chem. Rev.* **1999**, *99*, 1849.
(3) Haynes, C. L.; Van Duyne, R. P. *J. Phys. Chem. B* **2001**, *105*, 5599.
(4) Xia, Y. N.; Yang, P. D.; Sun, Y. G.; Wu, Y. Y.; Mayers, B.; Gates, B.; Yin, Y. D.; Kim, F.; Yan, Y. Q. *Adv. Mater.* **2003**, *15*, 353.
(5) Murphy, C. J.; San, T. K.; Gole, A. M.; Orendorff, C. J.; Gao, J. X.; Gou, L.; Hunyadi, S. E.; Li, T. *J. Phys. Chem. B* **2005**, *109*, 13857.
(6) Perez-Juste, J.; Pastoriza-Santos, I.; Liz-Marzan, L. M.; Mulvaney, P. *Coord. Chem. Rev.* **2005**, *249*, 1870.
(7) Burda, C; Chen, X. B.; Narayanan, R; El-Sayed, M. A. *Chem. Rev.* **2005**, *105*, 1025.
(8) Pileni, M. P. *J. Phys. Chem. C* **2007**, *111*, 9019.
(9) Wang, H.; Brandl, D. W.; Nordlander, P.; Halas, N. J. *Acc. Chem. Res.* **2007**, *40*, 53.
(10) Schwartzberg, A. M.; Zhang, J. Z. *J. Phys. Chem. C* **2008**, *112*, 10323.
(11) Rosi, N. L.; Mirkin, C. A. *Chem. Rev.* **2005**, *105*, 154.
(12) Cheng, M. M. C.; Cuda, G.; Bunimovich, Y. L.; Gaspari, M.; Heath, J. R.; Hill, H. D.; Mirkin, C. A.; Nijdam, A. J.; Terracciano, R.; Thundat, T.; Ferrari, M. *Curr. Opin. Chem. Biol.* **2006**, *10*, 11.
(13) Willets, K. A.; Van Duyne, R. P. *Annu. Rev. Phys. Chem.* **2007**, *58*, 267.
(14) Schultz, D. A. *Curr. Opin. Biotech.* **2003**, *14*, 13.
(15) Nicewarner-Pena, S. R.; Freeman, R. G.; Reiss, B. D.; He, L.; Pena, D. J.; Walton, I. D.; Cromer, R.; Keating, C. D.; Natan, M. J. *Science* **2001**, *294*, 137.
(16) Raschke, G.; Kowarik., S.; Franzl, T.; Sonnichsen, C.; Klar, T. A.; Feldmann, J.; Nichtl, A.; Kurzinger, K. *Nano Lett.* **2003**, *3*, 935.
(17) Nehl, C. L.; Liao, H. W.; Hafner, J. H. *Nano Lett.* **2006**, *6*, 683.
(18) Bukasov, R.; Shumaker-Parry, J. S. *Nano Lett.* **2007**, *7*, 1113.
(19) Henzie, J.; Lee, M. H.; Odom, T. W. *Nature Nanotechnol.* **2007**, *2*, 549.
(20) Lu, Y.; Liu, G. L.; Kim, J.; Mejia, Y. X.; Lee, L. P. *Nano Lett.* **2005**, *5*, 119.
(21) Loo, C.; Lowery, A.; Halas, N. J.; West, J.; Drezek, R. *Nano Lett.* **2005**, *5*, 709.
(22) Huang, X. H.; El-Sayed, I. H.; Qian, W.; El-Sayed, M. A. *J. Am. Chem. Soc.* **2006**, *128*, 2115.
(23) Chen, J. Y.; Wang, D. L.; Xi, J. F.; Au, L.; Siekkinen, A.; Warsen, A.; Li, Z. Y.; Zhang, H.; Xia, Y. N.; Li, X. D. *Nano Lett.* **2007**, *7*, 1318.
(24) Huff, T. B.; Tong, L.; Zhao, Y.; Hansen, M. N.; Cheng, J. X.; Wei, A. *Nanomedicine* **2007**, *2*, 125.
(25) Gobin, A. M.; Lee, M. H.; Halas, N. J.; James, W. D.; Drezek, R. A.; West, J. L. *Nano Lett.* **2007**, *7*, 1929.
(26) Schwartzberg, A. M.; Zhang, J. Z. *J. Phys. Chem. C* **2008**, *112*, 10323.
(27) Murphy, C. J.; Gole, A. M.; Stone, J. W.; Sisco, P. N.; Alkilany, A. M.; Goldsmith, E. C.; Baxter, S. C. *Acc. Chem. Res.* **2008**, *41*, 1721.
(28) Hu, M.; Chen, J. Y.; Li, Z. Y.; Au, L.; Hartland, G. V.; Li, X. D.; Marquez, M.; Xia, Y. N. *Chem. Soc. Rev.* **2006**, *35*, 1084.
(29) Maier, S. A.; Brongersma, M. L.; Kik, P. G.; Meltzer, S.; Requicha, A. A. G.; Atwater, H. A. *Adv. Mater.* **2001**, *13*, 1501.
(30) Maier, S. A.; Kik, P. G.; Atwater, H. A.; Meltzer, S.; Harel, E.; Koel, B. E.; Requicha, A. A. G. *Nat. Mater.* **2003**, *2*, 229.
(31) Barnes, W. L.; Dereux, A.; Ebbesen, T. W. *Nature* **2003**, *424*, 824.
(32) Bozhevolnyi, S. I.; Volkov, V. S.; Devaux, E.; Laluet, J. Y.; Ebbesen, T. W. *Nature* **2006**, *440*, 508.
(33) Kreibig, U.; Vollmer, M. *Optical Properties of Metal Clusters*; Springer-Verlag: Berlin, 1995.
(34) Mulvaney, P. *Langmuir* **1996**, *12*, 788.
(35) Kelly, K. L.; Coronado, E.; Zhao, L. L.; Schatz, G. C. *J. Phys. Chem. B* **2003**, *107*, 668.
(36) van de Hulst, H. C. *Light Scattering by Small Particles*; Dover: New York, 1981.
(37) Bohren, C. F.; Huffman, D. R. *Absorption and Scattering of Light by Small Particles*; Wiley-Interscience: New York, 1983.
(38) Link, S.; El-Sayed, M. A. *J. Phys. Chem. B* **1999**, *103*, 8410.
(39) Link, S.; El-Sayed, M. A. *Int. Rev. Phys. Chem.* **2000**, *19*, 409.
(40) Zhang, J. Z. *Acc. Chem. Res.* **1997**, *30*, 423.
(41) Voisin, C.; Del Fatti, N.; Christofilos, D.; Vallee, F. *J. Phys. Chem. B* **2001**, *105*, 2264.
(42) Hodak, J. H.; Henglein, A.; Hartland, G. V. *J. Phys. Chem. B* **2000**, *104*, 9954.
(43) Hartland, G. V. *Int. J. Nanotechnol.* **2004**, *1*, 307.
(44) Lu, X. M.; Rycenga, M.; Skrabalak, S. E.; Wiley, B.; Xia, Y. N. *Annu. Rev. Phys. Chem.* **2009**, *60*, 167.
(45) Grzelczak, M.; Perez-Juste, J.; Mulvaney, P.; Liz-Marzan, L. M. *Chem. Soc. Rev.* **2008**, *37*, 1783.
(46) Steinfeld, J. I. *Molecules and Radiation: An Introduction to Modern Molecular Spectroscopy*; MIT Press: Cambridge, MA, 1985.
(47) El-Sayed, M. A *Acc. Chem. Res.* **2004**, *37*, 326.
(48) Klimov, V. I. *J. Phys. Chem. B* **2000**, *104*, 6112.
(49) Prasankumar, R. P.; Upadhya, P. C.; Taylor, A. J. *Phys. Status Solidi B* **2009**, *246*, 1973.
(50) Mie, G. *Ann. Phys. (Weinheim, Ger.)* **1908**, *25*, 377.
(51) Ashcroft, N. W.; Mermin, N. D. *Solid State Physics*; Holt, Rinehart & Winston: New York, 1976.
(52) Kittel, C. *Introduction to Solid State Physics*; Wiley: Hoboken, NJ, 2005.
(53) Johnson, P. B.; Christy, R. W. *Phys. Rev. B* **1972**, *6*, 4370.
(54) Johnson, P. B.; Christy, R. W. *Phys. Rev. B* **1974**, *9*, 5056.
(55) Papaconstantopoulos, D. A. *Handbook of the Band Structure of Elemental Solids*; Plenum: New York, 1986.
(56) Alvarez, M. M.; Khoury, J. T.; Schaaff, T. G.; Shafigullin, M. N.; Vezmar, I.; Whetten, R. L. *J. Phys. Chem. B* **1997**, *101*, 3706.
(57) Kreibig, U. *J. Phys. F: Met. Phys.* **1974**, *4*, 999.
(58) Genzel, L.; Martin, T. P.; Kreibig, U. *Z. Phys. B* **1975**, *21*, 339.
(59) Kraus, W. A.; Schatz, G. C. *J. Chem. Phys.* **1983**, *79*, 6130.
(60) Coronado, E. A.; Schatz, G. C. *J. Chem. Phys.* **2003**, *119*, 3926.
(61) Kreibig, U.; Genzel, L. *Surf. Sci.* **1985**, *156*, 678.
(62) Liu, M. Z.; Guyot-Sionnest, P. *J. Phys. Chem. B* **2004**, *108*, 5882.

(63) Ehrenreich, H.; Philipp, H. R. *Phys. Rev.* **1962**, *128*, 1622.
(64) Noguez, C. *J. Phys. Chem. C* **2007**, *111*, 3806.
(65) Quinten, M. *Z. Phys. B: Condens. Matter Quanta* **1996**, *101*, 211.
(66) de Abajo, F. J. G. *J. Phys. Chem. C* **2008**, *112*, 17983.
(67) McMahon, J. M.; Gray, S. K.; Schatz, G. C. *Phys. Rev. Lett.* **2009**, *103*, 097403.
(68) McMahon, J. M.; Gray, S. K.; Schatz, G. C. *Phys. Rev. B* **2010**, *82*, 035423.
(69) (a) Kubo, R. *J. Phys. Soc. Jpn.* **1962**, *17*, 975. (b) Kawabata, A.; Kubo, R. *J. Phys. Soc. Jpn.* **1966**, *21*, 1765.
(70) Kubo, R.; Kawabata, A.; Kobayashi, S. *Annu. Rev. Mater. Sci.* **1984**, *14*, 49.
(71) Schaaff, T. G.; Shafigullin, M. N.; Khoury, J. T.; Vezmar, I.; Whetten, R. L.; Cullen, W. G.; First, P. N.; Gutierrez Wing, C.; Ascensio, J.; Jose Yacaman, M. J. *J. Phys. Chem. B* **1997**, *101*, 7885.
(72) Schaaff, T. G.; Knight, G.; Shafigullin, M. N.; Borkman, R. F.; Whetten, R. L. *J. Phys. Chem. B* **1998**, *102*, 10643.
(73) Smith, B. A.; Zhang, J. Z.; Giebel, U.; Schmid, G. *Chem. Phys. Lett.* **1997**, *270*, 139.
(74) Link, S.; El-Sayed, M. A.; Schaaff, T. G.; Whetten, R. L. *Chem. Phys. Lett.* **2002**, *356*, 240.
(75) Varnavski, O.; Ramakrishna, G.; Kim, J.; Lee, D.; Goodson, T. *J. Am. Chem. Soc.* **2010**, *132*, 16.
(76) Link, S.; Wang, Z. L.; El-Sayed, M. A. *J. Phys. Chem. B* **1999**, *103*, 3529.
(77) Gans, R. *Ann. Phys.* **1915**, *47*, 270.
(78) (a) Link, S.; Mohamed, M. B.; El-Sayed, M. A. *J. Phys. Chem. B* **1999**, *103*, 3073. (b) Link, S.; El-Sayed, M. A.; Mohamed, M. B. *J. Phys. Chem. B* **2005**, *109*, 10531.
(79) Yan, B. H.; Yang, Y.; Wang, Y. C. *J. Phys. Chem. B* **2003**, *107*, 9159.
(80) Prescott, S. W.; Mulvaney, P *J. Appl. Phys.* **2006**, *99*, 123504.
(81) Draine, B. T.; Flatau, P. J. *J. Opt. Soc. Am. A* **2008**, *25*, 2693.
(82) Draine, B. T.; Flatau, P. J. *J. Opt. Soc. Am. A* **1994**, *11*, 1491.
(83) Jensen, T.; Kelly, L.; Lazarides, A.; Schatz, G. C. *J. Cluster Sci.* **1999**, *10*, 295.
(84) Zhao, J.; Pinchuk, A. O.; McMahon, J. M.; Li, S. Z.; Ausman, L. K.; Atkinson, A. L.; Schatz, G. C. *Acc. Chem. Res.* **2008**, *41*, 1710.
(85) Wokaun, A.; Gordon, J. P.; Liao, P. F. *Phys. Rev. Lett.* **1982**, *48*, 957.
(86) Jackson, J. D. *Classical Electrodynamics*, John Wiley and Sons: New York, 1962.
(87) Sonnichsen, C.; Franzl, T.; Wilk, T.; von Plessen, G.; Feldmann, J.; Wilson, O.; Mulvaney., P. *Phys. Rev. Lett.* **2002**, *88*, 077402.
(88) Hu, M.; Novo, C.; Funston, A.; Wang, H. N.; Staleva, H.; Zou, S. L.; Mulvaney, P.; Xia, Y. N.; Hartland, G. V. *J. Mater. Chem.* **2008**, *18*, 1949.
(89) Sonnichsen, C.; Franzl, T.; Wilk, T.; von Plessen, G.; Feldmann, J. *New J. Phys.* **2002**, *4*, 93.
(90) Kuwata, H.; Tamaru, H.; Esumi, K.; Miyano, K. *Appl. Phys. Lett.* **2003**, *83*, 4625.
(91) Kreibig, U. *Appl. Phys.* **1976**, *10*, 255.
(92) Sargent, M.; Scully, M. O.; Lamb, W. E. *Laser Physics*; Addison-Wesley: Reading, MA, 1982.
(93) Novo, C.; Gomez, D.; Perez-Juste, J.; Zhang, Z. Y.; Petrova, H.; Reismann, M.; Mulvaney, P.; Hartland, G. V. *Phys. Chem. Chem. Phys.* **2006**, *8*, 3540.
(94) Liau, Y. H.; Unterreiner, A. N.; Chang, Q.; Scherer, N. F. *J. Phys. Chem. B* **2001**, *105*, 2135.
(95) Pelton, M.; Liu, M. Z.; Park, S.; Scherer, N. F.; Guyot-Sionnest, P. *Phys. Rev. B* **2006**, *73*, 155419.
(96) Sun, C. K.; Vallee, F.; Acioli, L. H.; Ippen, E. P.; Fujimoto, J. G. *Phys. Rev. B* **1994**, *50*, 15337.
(97) Del Fatti, N.; Voisin, C.; Achermann, M.; Tzortzakis, S.; Christofilos, D.; Vallee, F. *Phys. Rev. B* **2000**, *61*, 16956.
(98) Fann, W. S.; Storz, R.; Tom, H. W. K.; Bokor, J. *Phys. Rev. Lett.* **1992**, *68*, 2834.
(99) Fann, W. S.; Storz, R.; Tom, H. W. K.; Bokor, J. *Phys. Rev. B* **1992**, *46*, 13592.
(100) Voisin, C.; Christofilos, D.; Del Fatti, N.; Vallee, F.; Prevel, B.; Cottancin, E.; Lerme, J.; Pellarin, M.; Broyer, M. *Phys. Rev. Lett.* **2000**, *85*, 2200.
(101) Link, S.; Burda, C.; Mohamed, M. B.; Nikoobakht, B.; El-Sayed, M. A. *Phys. Rev. B* **2000**, *61*, 6086.
(102) Kaganov, M. I.; Lifshitz, I. M.; Tanatarov, L. V. *Zh. Eksp. Teor. Fiz.* **1957**, *31*, 232.
(103) Eesley, G. L. *Phys. Rev. Lett.* **1983**, *51*, 2140.
(104) Brorson, S. D.; Fujimoto, J. G.; Ippen, E. P. *Phys. Rev. Lett.* **1987**, *59*, 1962.
(105) Hohlfeld, J.; Wellershoff, S. S.; Gudde, J.; Conrad, U.; Jahnke, V.; Matthias, E. *Chem. Phys.* **2000**, *251*, 237.
(106) Hodak, J. H.; Martini, I.; Hartland, G. V. *Chem. Phys. Lett.* **1998**, *284*, 135.
(107) Hodak, J. H.; Henglein, A.; Hartland, G. V. *J. Chem. Phys.* **2000**, *112*, 5942.
(108) Hartland, G. V. *Annu. Rev. Phys. Chem.* **2006**, *57*, 403.
(109) Feldstein, M. J.; Keating, C. D.; Liau, Y. H.; Natan, M. J.; Scherer, N. F. *J. Am. Chem. Soc.* **1997**, *119*, 6638.
(110) Del Fatti, N.; Vallee, F.; Flytzanis, C.; Hamanaka, Y.; Nakamura, A. *Chem. Phys.* **2000**, *251*, 215.
(111) Arbouet, A.; Voisin, C.; Christofilos, D.; Langot, P.; Del Fatti, N.; Vallee, F.; Lerme, J.; Celep, G.; Cottancin, E.; Gaudry, M.; Pellarin, M.; Broyer, M.; Maillard, M.; Pileni, M. P.; Treguer, M. *Phys. Rev. Lett.* **2003**, *90*, 177401.
(112) Groeneveld, R. M. H.; Sprik, R.; Lagendijk, A. *Phys. Rev. B* **1995**, *51*, 11433.
(113) Hodak, J. H.; Henglein, A.; Hartland, G. V. *J. Chem. Phys.* **2001**, *114*, 2760.
(114) Chang, S. S.; Shih, C. W.; Chen, C. D.; Lai, W. C.; Wang, C. R. C. *Langmuir* **1999**, *15*, 701.
(115) Link, S.; Burda, C.; Mohamed, M. B.; Nikoobakht, B.; El-Sayed, M. A. *J. Phys. Chem. A* **1999**, *103*, 1165.
(116) Link, S.; Burda, C.; Nikoobakht, B.; El-Sayed, M. A. *J. Phys. Chem. B* **2000**, *104*, 6152.
(117) Kamat, P. V.; Flumiani, M.; Hartland, G. V. *J. Phys. Chem. B* **1998**, *102*, 3123.
(118) Takami, A.; Kurita, H.; Koda, S. *J. Phys. Chem. B* **1999**, *103*, 1226.
(119) Mafune, F.; Kohno, J.; Takeda, Y.; Kondow, T.; Sawabe, H. *J. Phys. Chem. B* **2000**, *104*, 9111.
(120) Hu, M.; Wang, X.; Hartland, G. V.; Mulvaney, P.; Perez-Juste, J.; Sader, J. E. *J. Am. Chem. Soc.* **2003**, *125*, 14925.
(121) Nisoli, M.; DeSilvestri, S.; Cavalleri, A.; Malvezzi, A. M.; Stella, A.; Lanzani, G.; Cheyssac, P.; Kofman, R. *Phys. Rev. B* **1997**, *55*, 13424.
(122) Hodak, J. H.; Martini, I.; Hartland, G. V. *J. Chem. Phys.* **1998**, *108*, 9210.
(123) Del Fatti, N.; Voisin, C.; Chevy, F.; Vallee, F.; Flytzanis, C. *J. Chem. Phys.* **1999**, *110*, 11484.
(124) Hodak, J. H.; Henglein, A.; Hartland, G. V. *J. Chem. Phys.* **1999**, *111*, 8613.
(125) Perner, M.; Gresillon, S.; Marz, J.; von Plessen, G.; Feldmann, J.; Porstendorfer, J.; Berg, K. J.; Berg, G. *Phys. Rev. Lett.* **2000**, *85*, 792.
(126) Voisin, C.; Del Fatti, N.; Christofilos, D.; Vallee, F. *Appl. Surf. Sci.* **2000**, *164*, 131.
(127) Pelton, M.; Sader, J. E.; Burgin, J.; Liu, M. Z.; Guyot-Sionnest, P.; Gosztola, D. *Nat. Nanotechnol.* **2009**, *4*, 492.
(128) Hartland, G. V. *J. Chem. Phys.* **2002**, *116*, 8048.
(129) Hartland, G. V. *Phys. Chem. Chem. Phys.* **2004**, *6*, 5263.
(130) van Dijk, M. A.; Lippitz, M.; Orrit, M. *Phys. Rev. Lett.* **2005**, *95*, 267406.
(131) Muskens, O. L.; Del Fatti, N.; Vallee, F. *Nano Lett.* **2006**, *6*, 552.
(132) van Dijk, M. A.; Lippitz, M.; Stolwijk, D.; Orrit, M. *Opt. Express* **2007**, *15*, 2273.
(133) Wilson, O. M.; Hu, X. Y.; Cahill, D. G.; Braun, P. V. *Phys. Rev. B* **2002**, *66*, 224301.
(134) Ge, Z. B.; Cahill, D. G.; Braun, P. V. *J. Phys. Chem. B* **2004**, *108*, 18870.

(135) Plech, A.; Kotaidis, V.; Gresillon, S.; Dahmen, C.; von Plessen, G. *Phys. Rev. B* **2004**, *70*, 195423.
(136) Perrin, B. *Microscale Nanoscale Heat Transfer* **2007**, *107*, 333.
(137) Juve, V.; Scardamaglia, M.; Maioli, P.; Crut, A.; Merabia, S.; Joly, L.; Del Fatti, N.; Vallee, F. *Phys. Rev. B* **2009**, *80*, 195406.
(138) Tas, G.; Maris, H. J. *Phys. Rev. B* **1994**, *49*, 15046.
(139) Carslaw, H. S. *Conduction of Heat in Solids*; Clarendon Press: Oxford, 1959.
(140) Hu, M.; Hartland, G. V. *J. Phys. Chem. B* **2002**, *106*, 7029; **2003**, *107*, 1284.
(141) Ju, Y. S. *J. Heat Transfer* **2005**, *127*, 1400.
(142) Steubing, W. *Ann. Phys. (Weinheim, Ger.)* **1908**, *26*, 329.
(143) Fragstein, C. V.; Römer, H. *Z. Phys.* **1958**, *151*, 54.
(144) Hampe, W. *Z. Phys.* **1958**, *152*, 476.
(145) Doyle, W. T. *Phys. Rev.* **1958**, *111*, 1067.
(146) Doremus, R. H. *J. Chem. Phys.* **1964**, *40*, 2389.
(147) Doremus, R. H. *J. Chem. Phys.* **1965**, *42*, 414.
(148) Brust, M.; Walker, M.; Bethell, D.; Schiffrin, D. J.; Whyman, R. *Chem. Commun.* **1994**, 801.
(149) Leff, D. V.; Brandt, L.; Heath, J. R. *Langmuir* **1996**, *12*, 4723.
(150) Whetten, R. L.; Khoury, J. T.; Alvarez, M. M.; Murthy, S.; Vezmar, I.; Wang, Z. L.; Stephens, P. W.; Cleveland, C. L.; Luedtke, W. D.; Landman, U. *Adv. Mater.* **1996**, *8*, 428.
(151) Stoeva, S.; Klabunde, K. J.; Sorensen, C. M.; Dragieva, I. *J. Am. Chem. Soc.* **2002**, *124*, 2305.
(152) Henglein, A.; Meisel, D. *Langmuir* **1998**, *14*, 7392.
(153) Henglein, A. *Langmuir* **1999**, *15*, 6738.
(154) Weare, W. W.; Reed, S. M.; Warner, M. G.; Hutchison, J. E. *J. Am. Chem. Soc.* **2000**, *122*, 12890.
(155) Liu, M. Z.; Guyot-Sionnest, P. *J. Phys. Chem. B* **2005**, *109*, 22192.
(156) Burgin, J.; Liu, M. Z.; Guyot-Sionnest, P. *J. Phys. Chem. C* **2008**, *112*, 19279.
(157) Liu, M. Z.; Pelton, M.; Guyot-Sionnest, P. *Phys. Rev. B* **2009**, *79*, 035418.
(158) Sonnichsen, C.; Geier, S.; Hecker, N. E.; von Plessen, G.; Feldmann, J.; Ditlbacher, H.; Lamprecht, B.; Krenn, J. R.; Aussenegg, F. R.; Chan, V. Z. H.; Spatz, J. P.; Moller, M. *Appl. Phys. Lett.* **2000**, *77*, 2949.
(159) Schultz, S.; Smith, D. R.; Mock, J. J.; Schultz, D. A. *Proc. Natl. Acad. Sci. U.S.A.* **2000**, *97*, 996.
(160) Mock, J. J.; Barbic, M.; Smith, D. R.; Schultz, D. A.; Schultz, S. *J. Chem. Phys.* **2002**, *116*, 6755.
(161) McFarland, A. D.; Van Duyne, R. P. *Nano Lett.* **2003**, *3*, 1057.
(162) Sherry, L. J.; Chang, S. H.; Schatz, G. C.; Van Duyne, R. P.; Wiley, B. J.; Xia, Y. N. *Nano Lett.* **2005**, *5*, 2034.
(163) Becker, J.; Schubert, O.; Sonnichsen, C. *Nano Lett.* **2007**, *7*, 1664.
(164) Munechika, K.; Smith, J. M.; Chen, Y.; Ginger, D. S. *J. Phys. Chem. C* **2007**, *111*, 18906.
(165) Demtroder, W. *Laser Physics: Basic Concepts and Instrumentation*; Springer-Verlag: Berlin, 1982.
(166) Slaughter, L. S.; Chang, W. S.; Swanglap, P.; Tcherniak, A.; Khanal, B. P.; Zubarev, E. R.; Link, S. *J. Phys. Chem. C* **2010**, *114*, 4934.
(167) Nehl, C. L.; Grady, N. K.; Goodrich, G. P.; Tam, F.; Halas, N. J.; Hafner, J. H. *Nano Lett.* **2004**, *4*, 2355.
(168) Wiley, B. J.; Chen, Y. C.; McLellan, J. M.; Xiong, Y. J.; Li, Z. Y.; Ginger, D.; Xia, Y. N. *Nano Lett.* **2007**, *7*, 1032.
(169) Hao, F.; Nehl, C. L.; Hafner, J. H.; Nordlander, P. *Nano Lett.* **2007**, *7*, 729.
(170) Rodriguez-Fernandez, J.; Novo, C.; Myroshnychenko, V.; Funston, A. M.; Sanchez-Iglesias, A.; Pastoriza-Santos, I.; Perez-Juste, J.; de Abajo, F. J. G.; Liz-Marzan, L. M.; Mulvaney, P. *J. Phys. Chem. C* **2009**, *113*, 18623.
(171) Oubre, C.; Nordlander, P. *J Phys. Chem. B* **2004**, *108*, 17740.
(172) Oubre, C.; Nordlander, P. *J Phys. Chem. B* **2005**, *109*, 10042.
(173) Yang, L. L.; Yan, B.; Reinhard, B. M. *J Phys. Chem. C* **2008**, *112*, 15989.
(174) Hu, M.; Chen, J. Y.; Marquez, M.; Xia, Y. N.; Hartland, G. V. *J Phys. Chem. C* **2007**, *111*, 12558.
(175) Mojarad, N. M.; Sandoghdar, V.; Agio, M. *J. Opt. Soc. Am. B* **2008**, *25*, 651.
(176) Mojarad, N. M.; Zumofen, G.; Sandoghdar, V.; Agio, M. *J. Eur. Opt. Soc.* **2009**, *4*, 09014.
(177) Knight, M. W.; Fan, J.; Capasso, F.; Halas, N. J. *Opt. Express* **2010**, *18*, 2579.
(178) Mohamed, M. B.; Volkov, V.; Link, S.; El-Sayed, M. A. *Chem. Phys. Lett.* **2000**, *317*, 517.
(179) Sherry, L. J.; Jin, R. C.; Mirkin, C. A.; Schatz, G. C.; Van Duyne, R. P. *Nano Lett.* **2006**, *6*, 2060.
(180) Hu, M.; Petrova, H.; Sekkinen, A. R.; Chen, J. Y.; McLellan, J. M.; Li, Z. Y.; Marquez, M.; Li, X. D.; Xia, Y. N.; Hartland, G. V. *J. Phys. Chem. B* **2006**, *110*, 19923.
(181) Berciaud, S.; Cognet, L.; Tamarat, P.; Lounis, B. *Nano Lett.* **2005**, *5*, 515.
(182) Wang, X.; Zhang, Z. Y.; Hartland, G. V. *J. Phys. Chem. B* **2005**, *109*, 20324.
(183) Becker, J.; Zins, I.; Jakab, A.; Khalavka, Y.; Schubert, O.; Sonnichsen, C. *Nano Lett.* **2008**, *8*, 1719.
(184) Henkel, A.; Jakab, A.; Brunklaus, G.; Sonnichsen, C. *J. Phys. Chem. C* **2009**, *113*, 2200.
(185) Banhart, J.; Czycholl, G. *Europhys. Lett.* **2002**, *58*, 264.
(186) Boyer, D.; Tamarat, P.; Maali, A.; Lounis, B.; Orrit, M. *Science* **2002**, *297*, 1160.
(187) Lindfors, K.; Kalkbrenner, T.; Stoller, P.; Sandoghdar, V. *Phys. Rev. Lett.* **2004**, *93*, 037401.
(188) Arbouet, A.; Christofilos, D.; Del Fatti, N.; Vallee, F.; Huntzinger, J. R.; Arnaud, L.; Billaud, P.; Broyer, M. *Phys. Rev. Lett.* **2004**, *93*, 127401.
(189) Berciaud, S.; Cognet, L.; Blab, G. A.; Lounis, B. *Phys. Rev. Lett.* **2004**, *93*, 257402.
(190) Jacobsen, V.; Stoller, P.; Brunner, C.; Vogel, V.; Sandoghdar, V. *Opt. Express* **2006**, *14*, 405.
(191) van Dijk, M. A.; Tchebotareva, A. L.; Orrit, M.; Lippitz, M.; Berciaud, S.; Lasne, D.; Cognet, L.; Lounis, B. *Phys. Chem. Chem. Phys.* **2006**, *8*, 3486.
(192) Cognet, L.; Tardin, C.; Boyer, D.; Choquet, D.; Tamarat, P.; Lounis, B. *Proc. Natl. Acad. Sci. U.S.A.* **2003**, *100*, 11350.
(193) Cognet, L.; Berciaud, S.; Lasne, D.; Lounis, B. *Anal. Chem.* **2008**, *80*, 2288.
(194) Berciaud, S.; Lasne, D.; Blab, G. A.; Cognet, L.; Lounis, B. *Phys. Rev. B* **2006**, *73*, 045424.
(195) Muskens, O. L.; Billaud, P.; Broyer, M.; Del Fatti, N.; Vallée, F *Phys. Rev. B* **2008**, *78*, 205410.
(196) Berciaud, S.; Cognet, L.; Lounis, B. *Phys. Rev. Lett.* **2008**, *101*, 077402.
(197) Giblin, J.; Syed, M.; Banning, M. T.; Kuno, M.; Hartland, G. *ACS Nano* **2010**, *4*, 358.
(198) Muskens, O. L.; Del Fatti, N.; Vallée, F.; Huntzinger, J. R.; Billaud, P.; Broyer, M. *Appl. Phys. Lett.* **2006**, *88*, 063109.
(199) Muskens, O.; Christofilos, D.; Del Fatti, N.; Vallee, F. *J. Opt. A: Pure Appl. Opt.* **2006**, *8*, S264.
(200) Billaud, P.; Huntzinger, J. R.; Cottancin, E.; Lerme, J.; Pellarin, M.; Arnaud, L.; Broyer, M.; Del Fatti, N.; Vallee, F. *Eur. Phys. J. D* **2007**, *43*, 271.
(201) Billaud, P.; Marhaba, S.; Cottancin, E.; Arnaud, L.; Bachelier, G.; Bonnet, C.; Del Fatti, N.; Lerme, J.; Vallee, F.; Vialle, J. L.; Broyer, M.; Pellarin, M. *J. Phys. Chem. C* **2008**, *112*, 978.
(202) Billaud, P.; Marhaba, S.; Grillet, N.; Cottancin, E.; Bonnet, C.; Lerme, J.; Vialle, J. L.; Broyer, M.; Pellarin, M. *Rev. Sci. Instrum.* **2010**, *81*, 043101.
(203) Muskens, O. L.; Bachelier, G.; Del Fatti, N.; Vallee, F.; Brioude, A.; Jiang, X. C.; Pileni, M. P. *J. Phys. Chem. C* **2008**, *112*, 8917.
(204) Gaiduk, A.; Ruijgrok, P. V.; Yorulmaz, M.; Orrit, M. *Chem. Sci.* **2010**, *1*, 343.
(205) Tcherniak, A.; Ha, J. W.; Dominguez-Medina, S.; Slaughter, L. S.; Link, S. *Nano Lett.* **2010**, *10*, 1398.

(206) Baida, H.; Billaud, P.; Marhaba, S.; Christofilos, D.; Cottancin, E.; Crut, A.; Lerme, J.; Maioli, P.; Pellarin, M.; Broyer, M.; Del Fatti, N.; Vallee, F.; Sanchez-Iglesias, A.; Pastoriza-Santos, I.; Liz-Marzan, L. M. *Nano Lett.* **2009**, *9*, 3463.
(207) Chang, W. S.; Ha, J. W.; Slaughter, L. S.; Link, S. *Proc. Nat. Acad. Sci. U.S.A.* **2010**, *107*, 2781.
(208) Voisin, C.; Christofilos, D.; Loukakos, P. A.; Del Fatti, N.; Valle, F.; Lerm, J.; Gaudry, M.; Cottancin, E.; Pellarin, M.; Broyer, M. *Phys. Rev. B* **2004**, *69*, 195416.
(209) Hache, F.; Ricard, D.; Flytzanis, C. *J. Opt. Soc. Am. B* **1986**, *3*, 1647.
(210) Hovel, H.; Fritz, S.; Hilger, A.; Kreibig, U.; Vollmer, M. *Phys. Rev. B* **1993**, *48*, 18178.
(211) Barnes, W. L.; Dereux, A.; Ebbesen, T. W. *Nature* **2003**, *424*, 824.
(212) Raether, H. *Surface Plasmons on Smooth and Rough Surfaces and on Gratings*; Springer-Verlag: Berlin, 1988.
(213) Krenn, J. R.; Lamprecht, B.; Ditlbacher, H.; Schider, G.; Salerno, M.; Leitner, A.; Aussenegg, F. R. *Europhys. Lett.* **2002**, *60*, 663.
(214) Ditlbacher, H.; Hohenau, A.; Wagner, D.; Kreibig, U.; Rogers, M.; Hofer, F.; Aussenegg, F. R.; Krenn, J. R. *Phys. Rev. Lett.* **2005**, *95*, 257403.
(215) Allione, M.; Temnov, V. V.; Fedutik, Y.; Woggon, U.; Artemyev, M. V. *Nano Lett.* **2008**, *8*, 31.
(216) Wiley, B. J.; Lipomi, D. I.; Bao, J. M.; Capasso, F.; Whitesides, G. M. *Nano Lett.* **2008**, *8*, 3023.
(217) *Surface Plasmon Resonance Based Sensors*; Homola, J., Ed.; Springer Series on Chemical Sensors and Biosensors, Vol. 4; Springer: Berlin, 2006.
(218) Dickson, R. M.; Lyon, R. A. *J. Phys. Chem. B* **2000**, *104*, 6095.
(219) Sanders, A. W.; Routenberg, D. A.; Wiley, B. J.; Xia, Y. N.; Dufresne, E. R.; Reed, M. A. *Nano Lett.* **2006**, *6*, 1822.
(220) Staleva, H.; Hartland, G. V. *Adv. Funct. Mater.* **2008**, *18*, 3809.
(221) Krenn, J. R.; Weeber, J. C.; Dereux, A.; Bourillot, E.; Goudonnet, J. P.; Schider, B.; Leitner, A.; Aussenegg, F. R.; Girard, C. *Phys. Rev. B* **1999**, *60*, 5029.
(222) Knight, M. W.; Grady, N. K.; Bardhan, R.; Hao, F.; Nordlander, P.; Halas, N. J. *Nano Lett.* **2007**, *7*, 2346.
(223) Pyayt, A. L.; Wiley, B.; Xia, Y. N.; Chen, A.; Dalton, L. *Nature Nanotechnol.* **2008**, *3*, 660.
(224) Yan, R.; Pausauskie, P.; Huang, J.; Yang, P. *Proc. Natl. Acad. Sci. U.S.A.* **2009**, *106*, 21045.
(225) Dong, C. H.; Ren, X. F.; Yang, R.; Duan, J. Y.; Guan, J. G.; Guo, G. C.; Guo, G. P. *Appl. Phys. Lett.* **2009**, *95*, 221109.
(226) Guo, X.; Qiu, M.; Bao, J. M.; Wiley, B. J.; Yang, Q.; Zhang, X. N.; Ma, Y. G.; Yu, H. K.; Tong, L. M. *Nano Lett.* **2009**, *9*, 4515.
(227) Ma, Y.; Li, X.; Yu, H.; Tong, L.; Gu, Y.; Gong, Q. *Opt. Lett.* **2010**, *35*, 1160.
(228) Schider, G.; Krenn, J. R.; Hohenau, A.; Ditlbacher, H.; Leitner, A.; Aussenegg, F. R.; Schaich, W. L.; Puscasu, I.; Monacelli, B.; Boreman, G. *Phys. Rev. B* **2003**, *68*, 155427.
(229) Charbonneau, R.; Berini, P.; Berolo, E.; Lisicka-Shrzek, E. *Opt. Lett.* **2000**, *25*, 844.
(230) Breukelaar, I.; Charbonneau, R.; Berini, P. *J. Appl. Phys.* **2006**, *100*, 043104.
(231) Tokizaki, T.; Nakamura, A.; Kaneko, S.; Uchida, K.; Omi, S.; Tanji, H.; Asahara, Y. *Appl. Phys. Lett.* **1994**, *65*, 941.
(232) Bigot, J. Y.; Merle, J. C.; Cregut, O.; Daunois, A. *Phys. Rev. Lett.* **1995**, *75*, 4702.
(233) Roberti, T. W.; Smith, B. A.; Zhang, J. Z. *J. Chem. Phys.* **1995**, *102*, 3860.
(234) Ahmadi, T. S.; Logunov, S. L.; El-Sayed, M. A. *J. Phys. Chem.* **1996**, *100*, 8053.
(235) Stella, A.; Nisoli, M.; DeSilvestri, S.; Svelto, O.; Lanzani, G.; Cheyssac, P.; Kofman, R. *Phys. Rev. B* **1996**, *53*, 15497.
(236) Nisoli, M.; Stagira, S.; DeSilvestri, S.; Stella, A.; Tognini, P.; Cheyssac, P.; Kofman, R. *Phys. Rev. Lett.* **1997**, *78*, 3575.
(237) Logunov, S. L.; Ahmadi, T. S.; El-Sayed, M. A.; Khoury, J. T.; Whetten, R. L. *J. Phys. Chem. B* **1997**, *101*, 3713.
(238) Lyons, L. *A Practical Guide to Data Analysis for Physical Science Students*; Cambridge University Press: Cambridge, U.K., 1993.
(239) Voisin, C.; Christofilos, D.; Loukakos, P. A.; Del Fatti, N.; Vallee, F.; Lerme, J.; Gaudry, M.; Cottancin, E.; Pellarin, M.; Broyer, M. *Phys. Rev. B* **2004**, *69*, 195416.
(240) Lerme, J.; Celep, G.; Broyer, M.; Cottancin, E.; Pellarin, M.; Arbouet, A.; Christofilos, D.; Guillon, C.; Langot, P.; Del Fatti, N.; Vallee, F. *Eur. Phys. J. D* **2005**, *34*, 199.
(241) Shahbazyan, T. V.; Perakis, I. E.; Bigot, J. Y. *Phys. Rev. Lett.* **1998**, *81*, 3120.
(242) Hodak, J. H.; Martini, I.; Hartland, G. V. *J. Phys. Chem. B* **1998**, *102*, 6958.
(243) Belotskii, E. D.; Tomchuk, P. M. *Surf. Sci.* **1990**, *239*, 143.
(244) Belotskii, E. D.; Tomchuk, P. M. *Int. J. Electron.* **1992**, *73*, 955.
(245) Darugar, Q.; Qian, W.; El-Sayed, M. A.; Pileni, M. P. *J. Phys. Chem. B* **2006**, *110*, 143.
(246) Park, S.; Pelton, M.; Liu, M.; Guyot-Sionnest, P.; Scherer, N. F. *J. Phys. Chem.C* **2007**, *111*, 116.
(247) Jiang, Y.; Wang, H. Y.; Xie, L. P.; Gao, I. R.; Wang, L.; Zhang, X. L.; Chen, Q. D.; Yang, H.; Song, H. W.; Sun, H. B. *J. Phys. Chem. C* **2010**, *114*, 2913.
(248) Knappenberger, K. L.; Schwartzberg, A. M.; Dowgiallo, A. M.; Lowman, C. A. *J. Am. Chem. Soc.* **2009**, *131*, 13892.
(249) Huang, W. Y.; Qian, W.; El-Sayed, M. A.; Ding, Y.; Wang, Z. L. *J. Phys. Chem. C* **2007**, *111*, 10751.
(250) Tang, Y.; Ouyang, M. *Nat. Mater.* **2007**, *6*, 754.
(251) Faulhaber, A. E.; Smith, B. A.; Andersen, J. K.; Zhang, J. Z. *Molec. Cryst. Liq. Cryst. Sci. Technol., A* **1996**, *283*, 25.
(252) Halte, V.; Bigot, J. Y.; Palpant, B.; Broyer, M.; Prevel, B.; Perez, A. *Appl. Phys. Lett.* **1999**, *75*, 3799.
(253) Link, S.; Hathcock, D. J.; Nikoobakht, B.; El-Sayed, M. A. *Adv. Mater.* **2003**, *15*, 393.
(254) Melinger, J. S.; Kleiman, V. A.; McMorrow, D.; Grohn, F.; Bauer, B. J.; Amis, E. *J. Phys. Chem. A* **2003**, *107*, 3424.
(255) Shin, H. J.; Hwang, I. W.; Hwang, Y. N.; Kim, D.; Han, S. H.; Lee, J. S.; Cho, G. J. *J. Phys. Chem. B* **2003**, *107*, 4699.
(256) Polavarapu, L.; Xu, Q. H. *Nanotechnology* **2009**, *20*, 185606.
(257) Link, S.; Burda, C.; Wang, Z. L.; El-Sayed, M. A. *J. Chem. Phys.* **1999**, *111*, 1255.
(258) Broyer, M.; Cottancin, E.; Lerme, J.; Pellarin, M.; Del Fatti, N.; Vallee, F.; Burgin, J.; Guillon, C.; Langot, P. *Faraday Discuss.* **2008**, *138*, 137.
(259) Enustun, B. V.; Turkevich, J. *J. Am. Chem. Soc.* **1963**, *85*, 3317.
(260) Gunnarsson, L.; Rindzevicius, T.; Prikulis, J.; Kasemo, B.; Kall, M.; Zou, S. L.; Schatz, G. C. *J. Phys. Chem. B* **2005**, *109*, 1079.
(261) Lassiter, J. B.; Aizpurua, J.; Hernandez, L. I.; Brandl, D. W.; Romero, I.; Lal, S.; Hafner, J. H.; Nordlander, P.; Halas, N. J. *Nano Lett.* **2008**, *8*, 1212.
(262) Lee, S. J.; Morrill, A. R.; Moskovits, M. *J. Am. Chem. Soc.* **2006**, *128*, 2200.
(263) Bosnick, K. A.; Jiang, J.; Brus, L. E. *J. Phys. Chem. B* **2002**, *106*, 8096.
(264) Jain, P. K.; Qian, W.; El-Sayed, M. A. *J. Phys. Chem. B* **2006**, *110*, 136.
(265) Ramakrishna, G.; Dai, Q.; Zou, J. H.; Huo, Q.; Goodson, T. *J. Am. Chem. Soc.* **2007**, *129*, 1848.
(266) Ingram, R. S.; Hostetler, M. J.; Murray, R. W.; Schaaff, T. G.; Khoury, J. T.; Whetten, R. L.; Bigioni, T. P.; Guthrie, D. K.; First, P. N. *J. Am. Chem. Soc.* **1997**, *119*, 9279.
(267) Chen, S. W.; Ingram, R. S.; Hostetler, M. J.; Pietron, J. J.; Murray, R. W.; Schaaff, T. G.; Khoury, J. T.; Alvarez, M. M.; Whetten, R. L. *Science* **1998**, *280*, 2098.
(268) Bigioni, T. P.; Whetten, R. L.; Dag, O. *J. Phys. Chem. B* **2000**, *104*, 6983.
(269) Huang, T.; Murray, R. W. *J. Phys. Chem. B* **2001**, *105*, 12498.
(270) Link, S.; Beeby, A.; FitzGerald, S.; El-Sayed, M. A.; Schaaff, T. G.; Whetten, R. L. *J. Phys. Chem. B* **2002**, *106*, 3410.
(271) Lee, D.; Donkers, R. L.; Wang, G. L.; Harper, A. S.; Murray, R. W. *J. Am. Chem. Soc.* **2004**, *126*, 6193.

(272) Negishi, Y.; Takasugi, Y.; Sato, S.; Yao, H.; Kimura, K.; Tsukuda, T. *J. Am. Chem. Soc.* **2004**, *126*, 6518.
(273) Wang, G. L.; Huang, T.; Murray, R. W.; Menard, L.; Nuzzo, R. G. *J. Am. Chem. Soc.* **2005**, *127*, 812.
(274) Shibu, E. S.; Muhammed, M. A. H.; Tsukuda, T.; Pradeep, T. *J. Phys. Chem. C* **2008**, *112*, 12168.
(275) Qian, H. F.; Zhu, Y.; Jin, R. C. *ACS Nano* **2009**, *3*, 3795.
(276) Hamanaka, Y.; Fukagawa, K.; Tai, Y.; Murakami, J.; Nakamura, A. *J. Lumin.* **2006**, *119*, 423.
(277) Ramakrishna, G.; Varnavski, O.; Kim, J.; Lee, D.; Goodson, T. *J. Am. Chem. Soc.* **2008**, *130*, 5032.
(278) Varnavski, O.; Ramakrishna, G.; Kim, J.; Lee, D.; Goodson, T. *ACS Nano* **2010**, *4*, 3406.
(279) Grant, C. D.; Schwartzberg, A. M.; Yang, Y. Y.; Chen, S. W.; Zhang, J. Z. *Chem. Phys. Lett.* **2004**, *383*, 31.
(280) Miller, S. A.; Womick, J. M.; Parker, J. F.; Murray, R. W.; Moran, A. M. *J. Phys. Chem. C* **2009**, *113*, 9440.
(281) Miller, S. A.; Fields-Zinna, C. A.; Murray, R. W.; Moran, A. M. *J. Phys. Chem. Lett.* **2010**, *1*, 1383.
(282) Heaven, M. W.; Dass, A.; White, P. S.; Holt, K. M.; Murray, R. W. *J. Am. Chem. Soc.* **2008**, *130*, 3754.
(283) Aikens, C. M. *J. Phys. Chem. C* **2008**, *112*, 19797.
(284) Seferyan, H. Y.; Zadoyan, R.; Wark, A. W.; Corn, R. M.; Apkarian, V. A. *J. Phys. Chem. C* **2007**, *111*, 18525.
(285) Petrova, H.; Lin, C. H.; de Liejer, S.; Hu, M.; McLellan, J. M.; Siekkinen, A. R.; Wiley, B. J.; Marquez, M.; Xia, Y. N.; Sader, J. E.; Hartland, G. V. *J. Chem. Phys.* **2007**, *126*, 094709.
(286) Simmons, G.; Wang, H. *Single Crystal Elastic Constants and Calculated Aggregate Properties: A Handbook*; MIT Press: Cambridge, MA, 1971.
(287) Dufey, F.; Fischer, S. F. *J. Phys. Chem. C* **2007**, *111*, 3868.
(288) Lamb, H. *Proc. Lond. Math. Soc.* **1882**, *13*, 189.
(289) Juve, V.; Crut, A.; Maioli, P.; Pellarin, M.; Broyer, M.; Del Fatti, N.; Vallee, F. *Nano Lett.* **2010**, *10*, 1853.
(290) Qian, H.; Steir, M.; Jin, R. *J. Phys. Chem. B* **2010**, *114*, 19935.
(291) Cerullo, G.; De Silvestri, S.; Banin, U. *Phys. Rev. B* **1999**, *60*, 1928.
(292) Chen, T. Y.; Hsia, C. H.; Son, H. S.; Son, D. H. *J. Am. Chem. Soc.* **2007**, *129*, 10829.
(293) Huxter, V. M.; Lee, A.; Lo, S. S.; Scholes, G. D. *Nano Lett.* **2009**, *9*, 405.
(294) McKimmie, L. J.; Lincoln, C. N.; Jasieniak, J.; Smith, T. A. *J. Phys. Chem. C* **2010**, *114*, 82.
(295) Hartland, G. V.; Hu, M.; Wilson, O.; Mulvaney, P.; Sader, J. E. *J. Phys. Chem. B* **2002**, *106*, 743.
(296) Burgin, J.; Langot, P.; Arbouet, A.; Margueritat, J.; Gonzalo, J.; Afonso, C. N.; Vallee, F.; Mlayah, A.; Rossell, M. D.; Van Tendeloo, G. *Nano Lett.* **2008**, *8*, 1296.
(297) Hu, M.; Petrova, H.; Wang, X.; Hartland, G. V. *J. Phys. Chem. B* **2005**, *109*, 14426.
(298) Bonacina, L.; Callegari, A.; Bonati, C.; van Mourik, F.; Chergui, M. *Nano Lett.* **2006**, *6*, 7.
(299) Yu, P.; Tang, J.; Lin, S. H. *J. Phys. Chem. C* **2008**, *112*, 17133.
(300) Hodak, J. H.; Henglein, A; Hartland, G. V. *J. Phys. Chem. B* **2000**, *104*, 5053.
(301) Guillon, C.; Langot, P.; Del Fatti, N.; Vallee, F.; Kirakosyan, A. S.; Shahbazyan, T. V.; Cardinal, T.; Treguer, M. *Nano Lett.* **2007**, *7*, 138.
(302) Shan, X.; Zhang, X.; Mazurenko, D. A.; van Blaaderen, A.; Dijkhuis, J. I.; Hudert, F.; Dekorsy, T. *J. Phys. Conf. Ser.* **2007**, *92*, 012035.
(303) Petrova, H.; Lin, C. H.; Hu, M.; Chen, J. Y.; Siekkinen, A. R.; Xia, Y. N.; Sader, J. E.; Hartland, G. V. *Nano Lett.* **2007**, *7*, 1059.
(304) Sando, G. M.; Berry, A. D.; Owrutsky, J. C. *J. Chem. Phys.* **2007**, *127*, 074704.
(305) Pomfret, M. B.; Brown, D. J.; Epshteyn, A.; Purdy, A. P.; Owrutsky, J. C. *Chem. Mater.* **2008**, *20*, 5945.
(306) Owrutsky, J. C.; Pomfret, M. B.; Brown, D. J. *J. Phys. Chem. C* **2009**, *113*, 10947.
(307) Jerebtsov, S. N.; Kolomenskii, A. A.; Liu, H. D.; Zhang, H.; Ye, Z. X.; Luo, Z. P.; Wu, W. H.; Paulus, G. G.; Schuessler, H. A. *Phys. Rev. B* **2007**, *76*, 184301.
(308) Kolomenskii, A. A.; Jerebtsov, S. N.; Liu, H. D.; Zhang, H.; Ye, Z. X.; Luo, Z. P.; Wu, W. H.; Schuessler, H. A. *J. Appl. Phys.* **2008**, *104*, 103110.
(309) Huang, W. Y.; Qian, W.; El-Sayed, M. A. *Nano Lett.* **2004**, *4*, 1741.
(310) Huang, W. Y.; Qian, W.; El-Sayed, M. A. *J. Phys. Chem. B* **2005**, *109*, 18881.
(311) Taubert, R.; Hudert, F.; Bartels, A.; Merkt, F.; Habenicht, A.; Leiderer, P.; Dekorsy, T. *New J. Phys.* **2007**, *9*, 376.
(312) Burgin, J.; Langot, P.; Del Fatti, N.; Vallee, F.; Huang, W.; El-Sayed, M. A. *J. Phys. Chem. C* **2008**, *112*, 11231.
(313) Huang, W. Y.; Qian, W.; Jain, P. K.; El-Sayed, M. A. *Nano Lett.* **2007**, *7*, 3227.
(314) Wang, L.; Nishijima, Y.; Ueno, K.; Misawa, H.; Tamai, N. *Appl. Phys. Lett.* **2009**, *95*, 053116.
(315) Crut, A.; Maioli, P.; Del Fatti, N.; Vallee, F. *Phys. Chem. Chem. Phys.* **2009**, *11*, 5882.
(316) Sader, J. E.; Hartland, G. V.; Mulvaney, P. *J. Phys. Chem. B* **2002**, *106*, 1399.
(317) Kirakosyan, A. S.; Shahbazyan, T. V. *J. Chem. Phys.* **2008**, *129*, 034708.
(318) Hu, M.; Hillyard, P.; Hartland, G. V.; Kosel, T.; Perez-Juste, J.; Mulvaney, P. *Nano Lett.* **2004**, *4*, 2493.
(319) Petrova, H.; Perez-Juste, J.; Zhang, Z. Y.; Zhang, J.; Kosel, T.; Hartland, G. V. *J. Mater. Chem.* **2006**, *16*, 3957.
(320) Zijlstra, P.; Tchebotareva, A. L.; Chon, J. W. M.; Gu, M.; Orrit, M. *Nano Lett.* **2008**, *8*, 3493.
(321) Hartland, G. V.; Hu, M.; Sader, J. E. *J. Phys. Chem. B* **2003**, *107*, 7472.
(322) Petrova, H.; Hu, M.; Hartland, G. V. *Z. Physik. Chem.* **2007**, *221*, 361.
(323) Plech, A.; Cerna, R.; Kotaidis, V.; Hudert, F.; Bartels, A.; Dekorsy, T. *Nano Lett.* **2007**, *7*, 1026.
(324) Hu, M.; Petrova, H.; Hartland, G. V. *Chem. Phys. Lett.* **2004**, *391*, 220.
(325) Petrova, H.; Perez-Juste, J.; Pastoriza-Santos, I.; Hartland, G. V.; Liz-Marzan, L. M.; Mulvaney, P. *Phys. Chem. Chem. Phys.* **2006**, *8*, 814.
(326) Hu, M.; Petrova, H.; Chen, J. Y.; McLellan, J. M.; Siekkinen, A. R.; Marquez, M.; Li, X. D.; Xia, Y. N.; Hartland, G. V. *J. Phys. Chem. B* **2006**, *110*, 1520.
(327) Chen, T. Y.; Hsia, C. H.; Son, D. H. *J. Phys. Chem. C* **2008**, *112*, 10125.
(328) Debenedetti, P. G. *Metastable Liquids: Concepts and Principles*, Princeton University Press: Princeton, NJ, 1996.
(329) Kotaidis, V.; Dahmen, C.; von Plessen, G.; Springer, F.; Plech, A. *J. Chem. Phys.* **2006**, *124*, 184702.
(330) Kotaidis, V.; Plech, A. *Appl. Phys. Lett.* **2005**, *87*, 213102.
(331) Lapotko, D. *Nanomedicine* **2009**, *4*, 813.
(332) Wijaya, A.; Schaffer, S. B.; Pallares, I. G.; Hamad-Schifferli, K. *ACS Nano* **2009**, *3*, 80.
(333) Gusev, V. E.; Wright, O. B. *Phys. Rev. B* **1998**, *57*, 2878.
(334) Perner, M.; Gresillon, S.; Marz, J.; von Plessen, G.; Feldmann, J.; Porstendorfer, J.; Berg, K. J.; Berg, G. *Phys. Rev. Lett.* **2000**, *85*, 792.
(335) Dubrovskiy, V. A.; Morochnik, V. S. *Earth Phys.* **1981**, *17*, 494.
(336) Saviot, L.; Netting, C. H.; Murray, D. B. *J. Phys. Chem. B* **2007**, *111*, 7457.
(337) Zener, C. *Phys. Rev.* **1937**, *52*, 230.
(338) Del Fatti, N.; Christofilos, D.; Vallee, F. *Gold Bull.* **2008**, *41*, 147.
(339) Staleva, H.; Hartland, G. V. *J. Phys. Chem. C* **2008**, *112*, 7535.
(340) Tchebotareva, A. L.; van Dijk, M. A.; Ruijgrok, P. V.; Fokkema, V.; Hesselberth, M. H. S.; Lippitz, M.; Orrit, M. *Chem. Phys. Chem.* **2009**, *10*, 111.
(341) Staleva, H.; Skrabalak, S. E.; Carey, C. R.; Kosel, T.; Xia, Y. N.; Hartland, G. V. *Phys. Chem. Chem. Phys.* **2009**, *11*, 5889.

(342) Cooper, F. *Int. J. Heat Mass. Trans* **1997**, *26*, 991.
(343) Plech, A.; Kurbitz, S.; Berg, K. J.; Graener, H.; Berg, G.; Gresillon, S.; Kaempfe, M.; Feldmann, J.; Wulff, M.; von Plessen, G. *Europhys. Lett.* **2003**, *61*, 762.
(344) Vardeman, C. F.; Gezelter, J. D. *J. Phys. Chem. C* **2008**, *112*, 3283.
(345) Schmidt, A. J.; Alper, J. D.; Chiesa, M.; Chen, G.; Das, S. K.; Hamad-Schifferli, K. *J. Phys. Chem. C* **2008**, *112*, 13320.
(346) Alpert, J.; Hamad-Schifferli, K. *Langmuir* **2010**, *26*, 3786.
(347) Ge, Z. B.; Kang, Y. J.; Taton, T. A.; Braun, P. V.; Cahill, D. G. *Nano Lett.* **2005**, *5*, 531.
(348) Hu, M.; Wang, X.; Hartland, G. V.; Salgueirino-Maceira, V.; Liz-Marzan, L. M. *Chem. Phys. Lett.* **2003**, *372*, 767.
(349) Dou, Y. S.; Zhigilei, L. V.; Winograd, N.; Garrison, B. J. *J. Phys. Chem. A* **2001**, *105*, 2748.
(350) Vardeman, C. F.; Conforti, P. F.; Sprague, M. M.; Gezelter, J. D. *J. Phys. Chem. B* **2005**, *109*, 16695.
(351) Merabia, S.; Shenogin, S.; Joly, L.; Keblinski, P.; Barrat, J. L. *Proc. Natl. Acad. Sci. U.S.A.* **2009**, *106*, 15113.